Adam Mickiewicz University in Poznań

The Faculty of Chemistry

DOCTORAL THESIS

mgr Adam Mieloch

Synthesis and analysis at the nanoscale. Biomedical applications of nanotechnology on the example of virus-like particles with a magnetic core and nanoindentation.

Synteza i analiza w skali *nano*. Biomedyczne zastosowania nanotechnologii na przykładzie cząstek wirusopodobnych z magnetycznym rdzeniem oraz nanoindentacji.

In the form of a collection of published and thematically related scientific articles

Promotor: prof. UAM dr hab. inż. Jakub D. Rybka

Poznań 2021

Streszczenie pracy w j. polskim

Głównym celem przeprowadzonych badań było zbadanie potencjału rozwiązań z obszaru syntezy i analizy w skali *nano*, do zastosowań biomedycznych. Część pracy dotycząca syntezy opiera się na otrzymywaniu i funkcjonalizacji superparamagnetycznych nanocząstek tlenku żelaza (SPION), ocenie ich właściwości biologicznych oraz wykorzystaniu do tworzenia cząstek wirusopodobnych (VLP) z magnetycznym rdzeniem. Część analityczna pracy oparta jest na nanoindentacji ludzkiej chrząstki stawu kolanowego objętej chorobą zwyrodnieniową stawów. Zaprezentowane wyniki podkreślają wysoki potencjał nanotechnologii w biomedycynie, wskazując jednocześnie pewne przeszkody na drodze do jej powszechnego zastosowania.

Pierwsza praca wchodząca w skład głównego osiągnięcia naukowego dotyczyła ewaluacji *in vitro* superparamagnetycznych nanocząstek tlenku żelaza funkcjonalizowanych diheksadecylofosoforanem (SPION-DHP). Otrzymane wyniki ukazują wysoki stopień biokompatybilności otrzymanych nanocząstek, czyniąc je obiecującym materiałem do zastosowań biomedycznych.

Druga praca wchodząca w skład głównego osiągnięcia naukowego dotyczyła tworzenia cząstek wirusopodobych z magnetycznym rdzeniem na bazie białka rdzeniowego wirusa zapalenia wątroby typu B oraz funkcjonalizowanych nanocząstek tlenku żelaza. W tym celu wykorzystano opisany w pierwszej pracy diheksadecylofosforan oraz inny związek funkcjonalizujący. Przeprowadzone badania pozwoliły na efektywne otrzymywanie cząstek wirusopodobnych z magnetycznym rdzeniem, stanowiąc istotny wkład w ten obszar nauki.

Trzecia praca wchodząca w skład głównego osiągnięcia naukowego dotyczyła analizy właściwości mechanicznych ludzkiej chrząstki stawowej pacjentów z chorobą poddanych zabiegowi całkowitej alloplastyki stawu kolanowego, oraz korelacji otrzymanych wyników ze stanem klinicznym pacjentów. Badanie zostało przeprowadzone na próbie 75 pacjentów. Otrzymane wyniki ukazują potencjał nanoindentacji do zastosowań w badaniach dotyczących progresji chorób degeneracyjnych powierzchni stawowych.

Podsumowując, prace wchodzące w skład głównego osiągnięcia naukowego dotyczą metod syntezy i analizy w skali *nano* do zastosowań w obszarach biomedycznych.

Table of Contents:

1. General goals of the thesis

The main goal of the presented research was to investigate the potential of nanoscale synthesis and analysis for biomedical applications. The synthetic part of the thesis is based on the synthesis and functionalization of superparamagnetic iron oxide nanoparticles (SPIONs), evaluation of their biological properties, and their utilization for the creation of virus-like particles (VLPs) with magnetic core. The analytical part of the thesis is based on the nanoindentation of human osteoarthritic knee joint cartilage. The conducted research highlights the yet untapped potential of nanotechnology in biomedicine while pinpointing certain hurdles on its way to widespread adoption.

2. Specific goals of particular core scientific achievements

In the first core scientific achievement, the aim was to conduct an *in vitro* evaluation of DHP-functionalized superparamagnetic iron oxide nanoparticles (SPION-DHP). The study included synthesis and functionalization of SPION-DHP, followed by a set of biological experiments aiming to evaluate biocompatibility of the obtained nanoparticles. The study included following biological analyses: cytotoxicity and proliferation assays, reactive oxygen species assay, SPIONs uptake analysis (*via* iron staining and ICP-MS), gene expression analysis. A set of the following genes was selected for the RT-qPCR analysis: alkaline phosphatase (ALPL); ferritin light chain (FTL); serine/threonine protein phosphatase 2A (PP2A); protein tyrosine phosphatase nonreceptor type 11 (PTPN11); transferrin receptor 1 (TFRC). The experiments were conducted on SW1353 (human chondrosarcoma) and TCam-2 (human seminoma) cancer derived cell lines.

In the second core scientific achievement, the goal was to obtain virus-like particles with a magnetic core composed of Hepatitis B virus core protein (HBc) and functionalized SPIONs. As the coating compound`s length and charge are crucial for the assembly efficacy and stability of the resulting VLPs, two compounds were selected for functionalization: 1,2-Distearoyl-sn-glycero-3-phosphoethanolamine-N-[carboxy-(polyethyleneglycol)-2000] and DHP. The HBc protein was obtained *via* agroinfection of *Nicotiana benthamiana* with pEAQ-HBc plasmid. The VLP assembly was evaluated with transmission electron microscopy and functionality testing (ELISA).

In the third core scientific achievement, a nanoindentation study was conducted on cartilage samples obtained from osteoarthritic patients subjected to the total knee replacement procedure. The main objective of this work was to investigate the correlation between patients` clinical state and the mechanical properties of the resected knee cartilage. This study has been conducted on a sample of 75 patients. The cartilage samples from both high weight bearing (HWB) and low weight bearing (LWB) femoral condyles were collected and subsequently analyzed *via* nanoindentation. There was no prior scientific data regarding the optimal sample preparation methodology, what is crucial for obtaining reliable data. The sample has to remain stable during the measurement, while maintaining high level of hydration, corresponding to physiological conditions. Additionally, the fixative should not interfere with mechanical properties of the sample. The evaluated mechanical properties were correlated with patients` clinical data and subjected to statistical analysis, providing insight into the progression of osteoarthritis.

In summary, the core scientific achievement is based on the application of nanotechnology in biomedicine, spanning from synthetic to analytical perspectives. The undertaken research encompasses a broad range of topics with a common denominator of "*nanotechnology in biomedicine*".

Core scientific achievements:

[1] **A.A. Mieloch**, M. Żurawek, M. Giersig, N. Rozwadowska, J.D. Rybka, *Bioevaluation of superparamagnetic iron oxide nanoparticles (SPIONs) functionalized with dihexadecyl phosphate (DHP).* Sci. Rep. (2020) 1–11. https://doi.org/10.1038/s41598-020-59478-2.
IF = 4.576 MNiSW = 140 pkt

[2] J.D. Rybka, **A.A. Mieloch***, A. Plis, M. Pyrski, T. Pniewski, M. Giersig, *Assembly and Characterization of HBc Derived Virus-like Particles with Magnetic Core.* Nanomater. (Basel, Switzerland). 9 (2019). https://doi.org/10.3390/nano9020155.
(* equally contributed)
IF = 4.324 MNiSW = 70 pkt

[3] **A.A. Mieloch**, M. Richter, T. Trzeciak, M. Giersig, J.D. Rybka, *Osteoarthritis Severely Decreases the Elasticity and Hardness of Knee Joint Cartilage: A Nanoindentation Study.* J. Clin. Med. 8 (2019) 1865. https://doi.org/10.3390/jcm8111865.
IF = 3.303 MNiSW = 140 pkt

Non-core scientific achievements:

[4] Szymański T, **Mieloch AA**, Richter M, Trzeciak T, Florek E, Rybka JD, Giersig M. Utilization of Carbon Nanotubes in Manufacturing of 3D Cartilage and Bone Scaffolds. Materials (Basel). 2020 Sep 11;13(18):4039. doi: 10.3390/ma13184039.
IF = 3.057 MNiSW = 100 pkt

[5] **A.A. Mieloch**, M. Kręcisz, J.D. Rybka, A. Strugała, M. Krupiński, A. Urbanowicz, M. Kozak, B. Skalski, M. Figlerowicz, M. Giersig, *The influence of ligand charge and length on the assembly of Brome mosaic virus derived virus-like particles with magnetic core.* AIP Adv. 8 (2018) 035005. https://doi.org/10.1063/1.5011138.
IF = 1.627 MNiSW = 70 pkt

[6] J.A. Semba, **A.A. Mieloch**, J.D. Rybka, *Introduction to the state-of-the-art 3D bioprinting methods, design, and applications in orthopedics.* Bioprinting. 18 (2020) e00070. https://doi.org/10.1016/j.bprint.2019.e00070.
MNiSW = 140 pkt

[7] M. Pyrski, **A.A. Mieloch**, A. Plewiński, A. Basińska-Barczak, A. Gryciuk, P. Bociag, M. Murias, J.D. Rybka, T. Pniewski, *Parenteral–oral immunization with plant-derived hbcag as a potential therapeutic vaccine against chronic hepatitis B*. Vaccines. 7 (2019). https://doi.org/10.3390/vaccines7040211.
IF = 4.086 MNiSW = 140 pkt

[8] **A.A. Mieloch**, W.M. Suchorska, *The concept of radiation-enhanced stem cell differentiation.* Radiol. Oncol. (2015). https://doi.org/10.1515/raon-2015-0022. **IF = 1.837 MNiSW = 70 pkt**

[9] Patent application: **A.A. Mieloch,** J.D. Rybka, F. Porzucek: “Hybrid nanoparticles binding antibodies, the method of their production and use for binding specific anti-SARS-CoV-2 antibodies”. **[WIPO ST 10/C PL437380]**

Bibliometric data:

Total IF = 22.81 Citations: 56 Total MNiSW = 870 pt H-index = 5

Other scientific achievements:

Conferences:

CELLINK Collaborative Partnership Conference, 2019, Milan, Italy	**Oral presentation**: "Mechanical properties of human osteoarthritic articular cartilage. Nanoindentation study"
NABIOMA 2018, Toruń, Poland	**Oral presentation**: "The influence of ligand charge and length on virus-like particles assembly with magnetic core." Honorable mention for the best presentation.
Nanotechnology in Biology and Medicine 2017, Warsaw, Poland	**Oral presentation**: "Design of viral-like particles with magnetic cores."
NanoWorld Conference 2017, Boston, USA	**Poster presentation:** 1." Assembly of virus-like nanoparticles with superparamagnetic core. Multifunctional platform for biomedical applications." 2. "Superparamagnetic iron oxide nanoparticles for bioimaging of myoblasts and mesechnymal stem cells for potential use in post-infraction heart stem cells therapy"

NANOMED 2016, Warsaw, Poland	**Oral presentation**: "Assembly of virus-like nanoparticles with superparamagnetic core. Multifunctional platform for biomedical applications."
nanoFORUM 2016, Serock, Poland	**Poster presentation:** 1. "Functionalization of superparamagnetic iron oxide nanoparticles (SPIONs) with dihexadecyl phosphate (DHP). A new solution to the old issue." 2. "Virus-like particles loaded with functionalized magnetite nanoparticles as a potential biomedical application." 3. "Superparamagnetic iron oxide nanoparticles for bioimaging of myoblasts and mesenchymal stem cells for potential use in post-infraction heart stem cell therapy."
7th International Conference of Contemporary Oncology 2015, Poznań, Poland	**Poster presentation:** "Radiobiological effects of radiation on embryoid bodies."
BIO 2014 Congress, Warsaw, Poland	**Poster presentation:** "Radiobiological effects of radiation on embryoid bodies."

Abroad internships:

01.08.2019 - 01.02.2020	**Internship at The Institute of Cancer Research, London, UK:** "The application of functionalized carbon nanotubes in near infrared photoimmunotherapy in the treatment of glioblastoma multiforme", under the supervision of dr Gabriela Kramer-Marek, Preclinical Molecular Imaging team.
15 - 19.2019	Summer School Utrecht: „3D Printing and Biofabrication."
20.07 - 02.08.2014	PLASMAG - Plasmonic and Magnetic Nanomaterials. Erasmus Intensive Programme. Freie University Berlin, Germany

Participation in research projects:

01.2021 -	**Researcher in the Single-name Hospitals (NCBiR) grant:** "Development and verification of the new COVID-19 Immunodiagnostic Tool". Dr hab. Jakub D. Rybka, prof. UAM as the principal investigator
01.2021 -	**Bioprinting Senior Researcher in the TECHMATSTRATEG (NCBiR) grant:** "Development of bioinks for 3D bioprinting based on chemically modified porcine dECM, enriched with recombinant hybrid proteins, nanomaterials, and synthetic polymers." Dr hab. Jakub D. Rybka, prof. UAM as the leader of the consortium part
11.2018 -	**Researcher in the LIDER (NCBiR) grant:** "MeniScaff 3D - 3D bioprinted, carbon nanotube-enhanced scaffolds for stimulated chondrogenic differentiation of mesenchymal stem cells for meniscus regeneration". Dr hab. Jakub D. Rybka, prof. UAM as the principal investigator
07.2017 - 09.2020	**Ph.D. student in the OPUS (NCN) grant:** "Synthesis, toxicological and functional studies on multi-walled carbon nanotubes as a scaffold for tissue engineering techniques in articular cartilage repair". Prof. dr hab. Michał Giersig as the principal investigator
07.2015 - 04.2017	**Researcher in the MAESTRO (NCN) grant:** "Targeted magnetic core viral shell particles". Prof. dr hab. Michał Giersig as the principal investigator
06.2014 - 06.2015	**The principal investigator of an internal grant** at Greater Poland Cancer Centre: "Radiobiological effects of radiation on embryoid bodies."

3. Scientific resume

After finishing education at the High School of the Insurgents of Greater Poland in Środa Wielkopolska, 09.2008, I started studying at the Medical-Vocational School in Poznań as a pharmacy technician, which I completed on 06.2010. Then, on 10.2010, I started the first degree studies at the Medical University of Karol Marcinkowski in Poznań in the field of Medical Biotechnology. I completed my BA thesis entitled "Impact of ionic liquid [CC] [MCPA] on apoptosis of A2780 cell lines derived from ovarian cancer" at the Department and Cell Biology Department under the supervision of dr Anna Szczerba in 07.2013. Then, I started my II degree studies on 10.2013 at the Faculty of Biology of the University of Adam Mickiewicz University in Poznań, majoring in Biotechnology - studies in English. I completed my master's thesis entitled "Radiobiological effects of ionizing radiation on embryoid bodies" at the Laboratory of Radiobiology, Greater Poland Cancer Centre in Poznań, under the supervision of dr hab. Wiktoria Suchorska. During my work, I received an internal grant of the same title, financed by the Greater Poland Cancer Centre. 20.08 - 02.08.2014 I took part in the intensive Erasmus program "PLASMAG - Plasmonic and Magnetic Nanomaterials. Erasmus Intensive Program Freie University Berlin, Germany." I received my master's degree in biotechnology on 09.2015. After completing my second degree studies, on 07.2015, I started working as a researcher in the MAESTRO project titled "Targeted magnetic core viral shell particles" under the supervision of prof. Michał Giersig. After the project`s completion in 04.2017, I became a Ph.D. student in the OPUS project by prof. Giersig, titled "Synthesis, toxicological and functional studies on multi-walled carbon nanotubes as a scaffold for tissue engineering techniques in articular cartilage repair". In parallel, 09.2017 I started Ph.D. studies at the Faculty of Chemistry at the University of Adam Mickiewicz in Poznań in the "ChemInter" course, implemented under the project POWR.03.02.00-00-I026/16.

I have been cooperating with prof. Jakub D. Rybka since 2015, which resulted in a jointly prepared grant application for the LIDER titled "MeniScaff 3D - 3D bioprinted carbon nanotube-enhanced scaffolds for stimulated chondrogenic differentiation of mesenchymal stem cells for meniscus regeneration", which obtained funding of 1 199 906 PLN, and in which I am employed since 11.2018 as the main co-investigator. In 2019, I took part in a summer school organized by Summer School Utrecht entitled "3D

Printing and Biofabrication". In the period from 01/08/2019 to 01/02/2020, I undertook a six-month internship at The Institute of Cancer Research, London, UK, under the supervision of prof. dr hab. Gabriela Kramer-Marek in the Preclinical Molecular Imaging team. During the internship, my research topics concerned the use of functionalized carbon nanotubes for near-infrared photoimmunotherapy in the treatment of glioblastoma multiforme.

In February 2020, together with prof. Rybka and the team, we decided to engage in the fight against the SARS-CoV-2 pandemic. As a result, we have co-authored a successful grant application titled “Development and verification of the new COVID-19 Immunodiagnostic Tool” funded by NCBiR under the “Single-name hospitals” call, acquiring 2 652 000 PLN. Since January 2021, I work in the project as a researcher. The results obtained during the first quarter allowed for patent application titled “Hybrid nanoparticles binding antibodies, the method of their production and use for binding specific anti-SARS-CoV-2 antibodies”. The ongoing work has been directed toward expanding the technology into other use cases.

The initiative has resulted in the creation of a research team composed of the Faculty of Biology at Adam Mickiewicz University (AMU), the Center for Advanced Technology at AMU, the Institute of Molecular Biology and Biotechnology at Poznań University of Medical Sciences (PUMS), and private companies: Cofactor and RobTech. The team is chaired by the Deputy Director of the AMU Center for Advanced Technologies, prof. Jakub D. Rybka.

The research initiated with the LIDER project resulted in a cooperation with the Foundation of Research and Science Development (FRSD) and the Medical University of Warsaw (MUW). Jointly with the FRSD and the MUW we have successfully applied for funding under TECHMATSTRATEG (NCBiR) call, with a grant proposal titled “Development of bioinks for 3D bioprinting based on chemically modified porcine dECM, enriched with recombinant hybrid proteins, nanomaterials and synthetic polymers”. The project acquired funding of 22 444 594 PLN. Currently, I work in the project as a Senior Bioprinting Specialist.

Adopting the term coined by the renowned French economist Frédéric Bastiat, my work can be divided into "*That Which is Seen and That Which is Not Seen*." The visible part being publications and conferences track record, while invisible being filed grant

applications. During my Ph.D. studies, I have co-authored more than fifteen grant applications, including such proposals as, e.g. LIDER, OPUS, POIR, TECHMATSTRATEG, MINIATURA, FirstTeam, from all major national agencies NCN, NCBiR, FNP, ABM, acquiring 26 296 500 PLN in total.

During my scientific journey, I have often undertaken new research topics, which always has resulted in broadening my scientific horizons. The wide range of subjects is reflected in the scope of my scientific achievements and ongoing research endeavors. Multidisciplinarity of research is one of the main currents of modern science, promoted by the most prestigious academic centers in the world. Presumably, quoting Shakespeare's Hamlet: "*there is a method in my madness,*" and the scientific path I choose to tread will lead to a holistic understanding of the Nature, rather than a chaotic and superficial experience of many subjects.

Time will tell.

4. Introduction

Nanotechnology is a rapidly developing field of multidisciplinary science, combining such fields as, e.g., chemistry, physics, biology. This work is focused on the synthesis and analysis at the nanoscale, on the example of virus-like particles (VLPs) with magnetic core and nanoindentation.

The biomedical applications of superparamagnetic iron oxide nanoparticles (SPIONs) is a topic that gained wide attention. Exceptional magnetic properties, high biocompatibility, precise size/shape control, and flexible surface modifications have led to many suitable solutions in magnetic hyperthermia, targeted drug delivery, magnetic resonance imaging (MRI) contrast, bioseparation, antimicrobial properties. Magnetic particle imaging (MPI) has recently emerged as a non-invasive imaging technique, based on SPIONs, which provides quantitative data rather than acting as an MRI contrasting agent. MPI can be utilized for cell tracking, tissue perfusion, and MPI-guided hyperthermia [1]. Iron oxide nanoparticles can also be effectively used as theranostic agents, combining targeted drug delivery, magnetic imaging, and local hyperthermia or thermal ablation [2]. SPIONs were also successfully used as photocatalyst and adsorbent in wastewater treatment [3]. In general, SPIONs can be viewed as multi-purpose particles, with

exceptional biocompatibility and outstanding functional design flexibility. The synthetic routes for SPIONs can be divided into two broad categories: top-down approach, and bottom-up approach.

The top-down approach focuses on a mechanical disruption of the bulk material through grinding and milling techniques. The milling can be divided into dry, and wet milling methods. A significant shortcoming of dry milling stems from a phenomenon known as “cold-welding”, in which the particles fuse together, forming larger aggregates. In this method, only sub-micrometer particles can be obtained [4]. Interestingly, an improved method of mechanical disruption called high-energy ball milling (HEBM) was shown to produce iron particles in 2-4 nm range [5]. To overcome the cold-welding effect without the need for increased kinetic energy, a wet milling method can be used. In this method, a water with or without surfactant is added to the milling jar, decreasing the surface energy of the particles, thus inhibiting the cold-welding. Using this method, 30 nm iron oxide nanoparticles were obtained [6]. Despite being environmentally friendly due to the lack of required solvents and chemicals, top-down approach of nanoparticles synthesis suffers from an inherent drawback of high polydispersity. Unfortunately, high levels of polydispersity disqualify nanoparticles from *in vivo* usage, as it directly affects various aspects of ADME (Adsorption, Metabolism, Elimination), making its` physiological faith unpredictable [7].

In turn, the bottom-up approach provides more controllable size distribution and also enables design of the surface properties *via* functionalization. There are several approaches to bottom-up synthesis including, but not limited to: co-precipitation, sol-gel reaction, sonochemical synthesis, hydrothermal synthesis, microemulsion reaction, thermal decomposition.

The thermal decomposition is not the most simplistic one, however, provides the highest degree of monodisperisty, colloidal stability, and scalability. In brief, the reaction of thermal decomposition of iron (III) acetylacetonate is performed under inert gas conditions (N_2, Ar), in an organic solvent (e.g. 1-octadecene), in the presence of surfactant(s) (e.g. oleic acid, oleylamine). The molar ratio between the $Fe(acac)_3$ and the surfactants is used to determine the size and shape of the resulting particles. Other factors such as time-at-temperature, solvent type, or gas flow rate may also affect the morphology of the SPIONs and have to be taken into consideration [8]. The main drawback

of this approach is the necessity for further functionalization as the resulted SPIONs are water insoluble. However, in my opinion the pros heavily outweigh cones, and therefore thermal decomposition was selected for the SPIONs synthesis.

As described above, SPIONs are an excellent choice for biomedical applications, and under this assumption, were selected for the core magnetic material for VLPs creation. The requirement of water solubility, highly negative surface charge, low production cost, and a straightforward functionalization route pinpointed several candidate coating compounds, from which dihexadecyl phosphate (DHP) was selected for SPIONs functionalization. Our previously published [**NSA 5**], successful utilization of DHP-coated SPIONs for VLPs creation has sparked our interest in detailing its biocompatibility, which has led to the publication listed as the first core scientific achievement [**CSA 1**].

Virus-like particles are constructs composed of viral proteins with an ordered structure (**Fig. 1**). Due to their native ability to self-assemble, structural proteins of the capsid are most commonly used for the VLPs creation. Importantly, VLPs are devoid of viral genetic material and, therefore, do not pose the risk of infection. Homo-multimeric construction of a capsid's subunits allows for relative ease of modification through standard techniques of protein engineering. A high degree of epitope ordering translates into high immunogenicity, which is particularly important for vaccines. Currently, there are several vaccines available on the market, developed based on VLP technology: Cervarix, Gardasil against HPV (human papillomavirus), Sci-B-Vac against HBV (hepatitis B virus) or Mosquirix against malaria [9]. Additionally, there is an ongoing development focused on multivalent vaccines, capable of presenting several antigens, characteristic of different viruses. For example, a vaccine prototype has been developed against Zika, Chikungunya, Yellow Fever, and Japanese Encephalitis, which share a common vector of infection – a mosquito [10]. Due to a high tissue specificity characteristic for viruses, VLPs can also be applied in targeted drug delivery [11]. For VLPs production, standard protein expression systems can be utilized, e.g., *e.coli*, yeasts, insects, plants, or mammalian cell lines [12].

Figure 1. *Schematic representation of a virus-like particle with magnetic core.*

The primary mechanism driving viral self-assembly is an electrostatic interaction between positively charged inward part of capsid subunits and negatively charged nucleic acid. This property allows for a substitution of the genetic material with other negatively charged functional constituents while maintaining the capacity for self-assembly. *In silico* simulations revealed a high complexity of the kinetics involved in this process. It was demonstrated that the introduction of a core in size commensurate with the inner diameter of a capsid, may facilitate the assembly and improve the overall stability of VLPs [13,14]. Additionally, the introduction of a core particle may provide extended functionality. In the second core scientific achievement [**CSA 2**], Hepatitis B virus core protein (HBc), and DHP functionalized iron oxide nanoparticles were used to create virus-like particles with a magnetic core.

Nanotechnology in biomedicine extends beyond the search of novel nanomaterials and synthetic routes, encompassing an equally promising field of analyses at the *nano* scale. The analytical aspect of this work is focused on the nanoindentation of human cartilage tissue. In general, indentation tests are performed to assess the mechanical properties of a sample and can be conducted at different scales (*macro, micro, nano*). Regardless of the scale, they are based on the same principle. A hard tip with defined mechanical properties is pushed into the sample. The load applied on the tip is gradually increased until reaching a previously specified value. The probe penetrates the sample to a specified depth and is subsequently removed from the material. During the whole process, the load applied and the displacement of the probe are recorded, resulting in a load-displacement curve (**Fig. 2**).

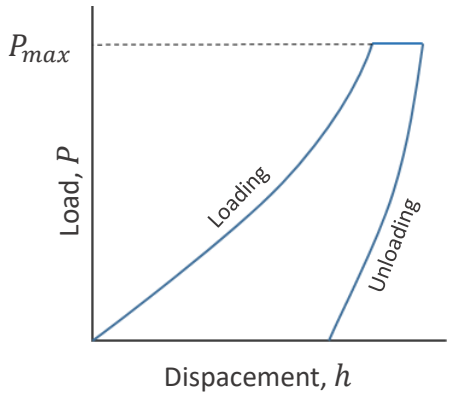

Figure 2. *Load-displacement curve.*

From the load-displacement curve, the mechanical properties of a sample can be derived. The hardness of a sample can be defined as relative resistance of the material's surface to penetration by a harder body. In order to calculate the hardness (H), an exact geometry of the probe has to be specified as it is defined as the maximum load (P_{max}), divided by the residual indentation area (A_r), according to the formula:

$$H = \frac{P_{max}}{A_r}$$

H – hardness
P_{max} – maximum load
A_r – residual indentation area

Another mechanical property that can be derived from the indentation technique is the Young's modulus, describing the stiffness of a sample. A solid material subjected to uniaxial loading (i.e., compression or extension) undergoes elastic deformation. As a result, the stress-strain curve can be obtained. The relationship between stress and strain in a linear elasticity regime describes the Young's modulus, summarized by the formula:

$$E = \frac{\sigma}{\varepsilon}$$

E – Young's modulus
σ – the uniaxial stress, or force per unit surface
ε – the strain or proportional deformation
The SI unit for the Young's modulus is the pascal (Pa), Pa = kg · m^{-1} · s^{-2}.

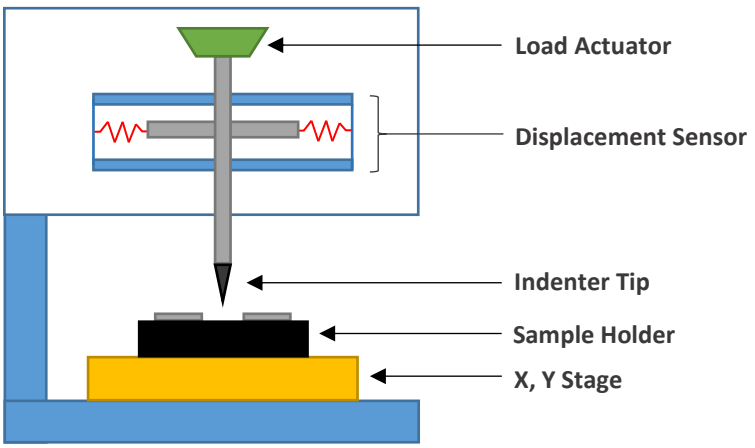

Figure 3. *Schematic representation of a nanoindenter.*

In nanoindentation, a modified version of the equation is used – the reduced Young's modulus, which includes the mechanical properties of the tip. The modulus is derived from the slope of the unloading phase of the load-displacement curve. Nanoindentation was developed to measure the hardness of materials at low volumes (**Fig. 3**). Most commonly, load actuators are based on magnetic coils, electrostatic force generators, or piezoelectric elements [15]. The displacement sensor can be capacitance or inductance based. An increasingly growing body of research indicates the relevance of tissue mechanics in disease progression, tissue remodeling, and regeneration. The main challenge in applying nanoindentation for testing biological materials stems from their complex and often hierarchical structure. In the case of layered materials, indentation depth is crucial for assessing the mechanical properties of a specific layer. Additionally, hydration of a sample has been shown to have a significant effect on its mechanical properties [16].

Biological samples are inherently non-homogenous, and therefore, establishing an exact thickness of a layer is a significant limitation of this method. Nanoindentation has been successfully used in the determination of the mechanical properties of such tissues as cortical bone, enamel, thoracic aorta, brain, or eye [17–21]. While hard tissues are relatively easy to analyze, soft tissues pose a significant challenge, due to viscoelastic properties and adhesion. The nanoindentation can be performed in quasi-static mode (slow loading phase, allowing for the system to retain internal equilibrium) or continuous stiffness measurement (CSM) mode. In CSM mode, an additional oscillatory load signal with a small amplitude and high frequency is applied throughout the whole loading phase. The main advantage of CSM over quasi-static mode is the ability to obtain hardness and elastic modulus throughout the whole loading phase, which is especially important for inhomogeneous and layered samples. In the third core scientific achievement [**CSA 3**], nanoindentation has been utilized to determine the mechanical properties of human cartilage, harvested from femoral condyles of patients diagnosed with osteoarthritis. The study was performed to define the relations between mechanical properties of the diseased cartilage and a clinical image of the patients after total knee replacement procedure.

5. Core achievements commentaries

Bioevaluation of superparamagnetic iron oxide nanoparticles (SPIONs) functionalized with dihexadecyl phosphate (DHP).

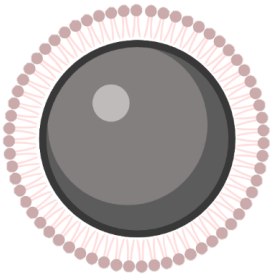

Figure 4. *Schematic representation of DHP-coated SPIONs.*

The aim of this work was to evaluate the biological properties of DHP-coated SPIONs. DHP functionalization provides SPIONs with negative surface charge and hydrophilic properties, which we have successfully utilized in our previous research regarding VLPs with magnetic core [**NSA 5**] (**Fig. 4**). My role in this work was multifaceted and included co-conceptualization of the experiments, synthesis, and functionalization of superparamagnetic iron oxide nanoparticles, sample preparation for inductively coupled plasma mass spectrometry analysis (ICP-MS), cytotoxicity study, data analysis, and manuscript preparation. The SPIONs were synthesized *via* thermal decomposition of iron (III) acetylacetonate $Fe(acac)_3$ with oleic acid as the surfactant. This method provides monodisperse SPIONs coated with oleic acid residues. The functionalization step with DHP is performed *via* phase transition approach. Briefly, DHP and SPIONs suspended in chloroform are mixed with hexane (organic phase). Subsequently, water is added, and the whole mixture is placed in a sonicating bath for several hours. As a result, DHP-coated SPIONs migrate into the water phase and can be easily extracted and purified for further use (**Fig. 5**). To obtain the precise measurement of the nanoparticles concentration, thermogravimetric analysis (TGA) was utilized. In short, a 20 µl sample was heated in the range of 20-150°C under nitrogen flow, to the point of the lowest mass. The density was calculated according to the formula $p = \frac{m}{V}$. The obtained SPION-DHP nanoparticles were administered to TCam-2 (human testicular seminoma) and SW1353 (human chondrosarcoma) cell lines. Proliferation and cytotoxicity assay was performed with commercially available CellTiter-Glo 2.0 assay (Promega). The assay determines the number of viable cells in culture by quantifying ATP, which indicates the presence of metabolically active cells. Luminescence readout is directly proportional to the number of viable cells in culture. The proliferation and

cytotoxicity were assessed 24h after SPION-DHP administration. Due to the inability to assess the cellular iron concentration *via* Prussian blue reaction, ICP-MS analysis was implemented. The method allowed for the quantitative determination of the nanoparticles uptake. The sample preparation requires freezing at -80°C, thawing and lysis with 10% SDS (sodium dodecyl sulfate), secondary freeze-thawing, sonication bath, and finally, dissolution in 65% nitric acid at 80°C. The samples were subsequently diluted ten-fold in DI water and used for measurement. Iron content was determined based on the standard curve prepared with a multielement standard solution for ICP-MS in the 1, 10, 100, 1000 ppb range.

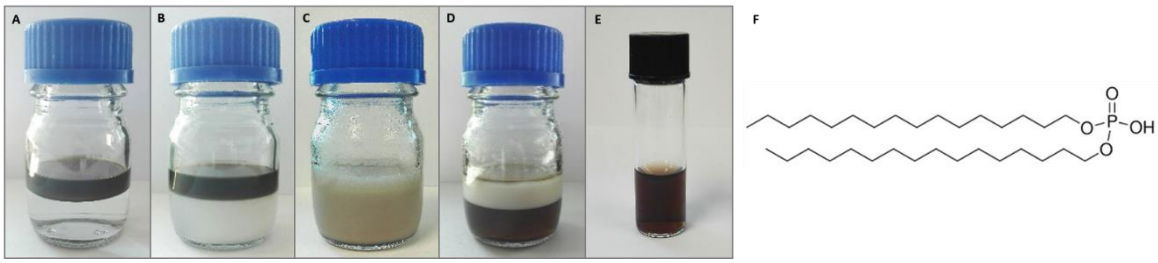

Figure 5. ***A*-*E*** *- sequential steps of SPIONs functionalization with DHP.* ***F*** *- structure of DHP*

In summary, this work was first to provide a detailed description of SPIONs functionalization with DHP and delve into the biological properties of the obtained nanoparticles. SPION-DHP nanoparticles did not reveal significant cytotoxicity in the range of tested concentrations, in selected cell lines. This preliminary investigation indicated that DHP-coated SPIONs may be safely utilized for biomedical applications.

Assembly and Characterization of HBc Derived Virus-like Particles with Magnetic Core.

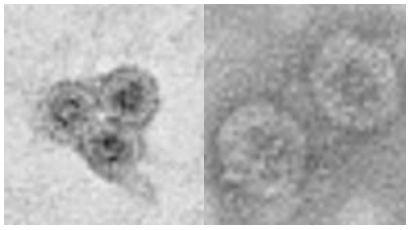

Figure 6. *HBc-derived VLPs with functionalizaed SPIONs as the magnetic core.*

The aim of this work was to utilize the hepatitis B virus core protein (HBc) to create virus-like particles (VLPs) with a magnetic core. My role in this project was co-conceptualization of the experiments, synthesis, and functionalization of superparamagnetic iron oxide nanoparticles, data analysis, and manuscript preparation. In this work, SPIONs were synthesized in the same way as described above. For the functionalization purposes, two compounds were used: 1,2-Distearoyl-sn-glycero-3-phosphoethanolamine-N-[carboxy-(polyethyleneglycol)-2000] (ammonium salt) (PL-PEG-COOH) and dihexadecyl phosphate (DHP). The mechanism of functionalization in both cases relies on hydrophobic interactions between alkyl chains of oleic acid residues present on the surface of SPIONs and alkyl chains of the compounds used. The DHP functionalization methodology is presented above. PL-PEG-COOH was performed as follows. PL-PEG-COOH was dissolved in chloroform and mixed with chloroform suspension of SPIONs. The mix was placed briefly in the sonicating bath, and the chloroform was subsequently evaporated. The obtained waxy solid was heated for 1 min in an 80°C water bath, and DI water was added, forming SPION-PL-PEG-COOH (SPION-PEG) nanoparticles. The solution was washed with chloroform to remove unbound PL-PEG-COOH, filtered, and subjected to further analysis. The concentration of both functionalized nanoparticles was assessed with TGA accordingly to the procedure described above. Both functionalizations resulted in negatively-charged nanoparticles, which is crucial for electrostatically-driven assembly of VLPs.

This work demonstrated the effects of ligands on the assembly of HBV derived virus-like particles with a magnetic core. In both cases, the successful creation of the VLPs was achieved (**Fig. 6**). The article expands on the magnetic core parameters governing the process of electrostatic self-assembly and furthers the knowledge on HBV based VLP systems. Considering the growing interest in utilizing VLP platforms for vaccine development, this research is relevant not only from the standpoint of basic but also applied science.

Osteoarthritis Severely Decreases the Elasticity and Hardness of Knee Joint Cartilage: A Nanoindentation Study.

The aim of this work was to evaluate the elasticity and hardness of the knee joint cartilage derived from patients diagnosed with osteoarthritis and subjected to a total knee replacement procedure. My role in this project was co-conceptualization of the experiments, developing a methodology for sample preparation for nanoindentation, conducting nanoindentation experiments, data analysis, and manuscript preparation. Nanoindentation is a highly precise measurement. Therefore sample preparation is essential for obtaining reliable data. Harvesting tissue samples from osteoarthritic cartilage for nanoindentation study is not a trivial matter. The damage may span from several osteophytes and slightly worn-out cartilage to a complete lack of cartilage tissue.

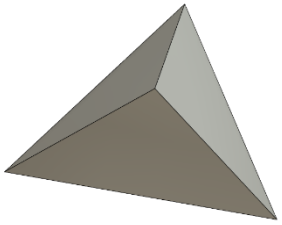

Figure 7. *Berkovich indentation tip model.*

Additionally, the variation between knee joint sizes hinders the selection of the same regions. A sample has to be horizontally and firmly placed in a holder. In the case of articular cartilage, which is highly hydrated tissue, ensuring water conditions for the whole measurement (ca. 3h) is a prerequisite. Taking all of the above into consideration, the acrylic resin was chosen for sample preparation. After fixation, samples were rehydrated

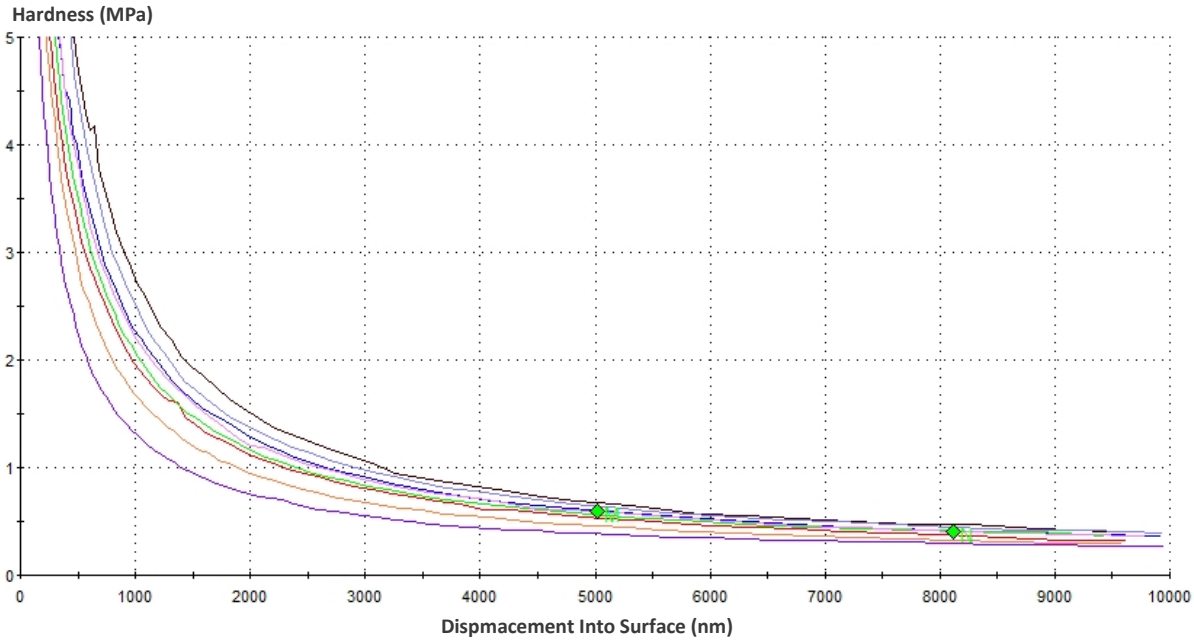

Figure 8. *An example of hardenss measurement. Colors represent separate indentations of one sample.*

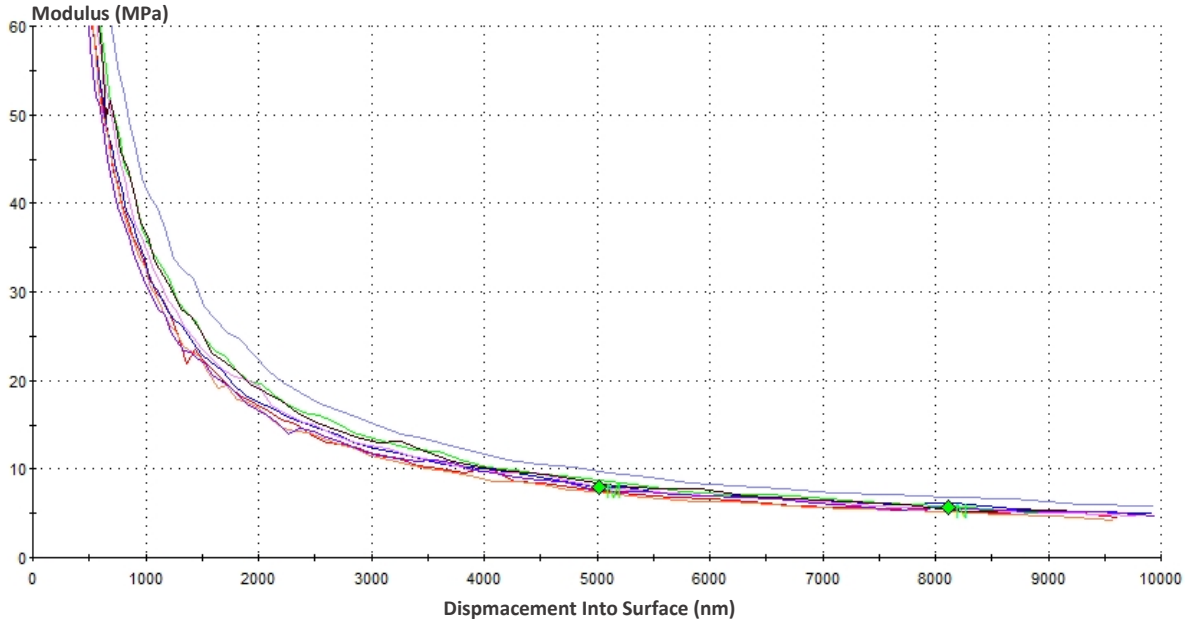

Figure 9. *An example of modulus measurement. Colors represent separate indentations of one sample.*

at RT with phosphate buffer saline (PBS) and subjected to nanoindentation analysis. The indentation tests were conducted on a nanoindenter Agilent G200 with a DCMII head fitted with a Berkovich-type indenter tip (**Fig. 7**). The tip was calibrated before each measurement on quartz crystal (Young's modulus E = 74 GPa).

The measurements were performed in CSM mode. The indentation depth was set at 10 µm at a strain rate of [1/s] the Poisson's ratio of 0,4. For each sample, 12 indents were performed in a 3 × 4 matrix with 200 µm X,Y indent separation. The hardness and mean elastic modulus were obtained from the 5.0–8.0 µm indentation depth range, which was established experimentally (**Fig. 8, 9**).

This work is one of the first studies of the nanomechanical properties of weight-bearing and non-weight-bearing articular cartilage at different stages of osteoarthritis conducted at this scale. The results provide insight into the mechanical behavior of the cartilage at different stages of osteoarthritis in correlation to the patients' ages, which is essential from the clinical perspective. It has also highlighted the limitations of this approach and provided practical guidelines to mitigate some of them.

6. Summary and perspectives

In regard to the core scientific achievements, to following conclusions can be drawn:

[**CSA 1**] **Bioevaluation of superparamagnetic iron oxide nanoparticles (SPIONs) functionalized with dihexadecyl phosphate (DHP).**

1. DHP-coated SPIONs did not reveal significant cytotoxicity in the range of tested concentrations.
2. SPION-DHP were successfully internalized by the cells, without eliciting significant alterations in gene expression profile of the selected genes.
3. Due to unknow reasons, iron staining is not compatible methodology for DHP-SPION detection.
4. SPION-DHP nanoparticles are a promising tool for biomedical applications.

[**CSA 2**] **Assembly and Characterization of HBc Derived Virus-like Particles with Magnetic Core.**

1. Both dihexadecyl phosphate and 1,2-distearoyl-sn-glycero-3-phosphoethanolamine-N-[carboxy-(polyethylene glycol)-2000] can be successfully used as functionalizing agents for the creation of HBc derived VLPs with magnetic core.
2. The obtained VLPs retained its ability to bind specific antibodies.
3. SPION-DHP displayed higher effectiveness in driving VLPs self-assembly.
4. The study provided meaningful insights into design and preparation of VLPs with magnetic core.

[**CSA 3**] **Osteoarthritis Severely Decreases the Elasticity and Hardness of Knee Joint Cartilage: A Nanoindentation Study.**

1. Nanoindentation requires careful experimental design including probe`s geometry, indentation depth, region of sample collection, and sample preparation methodology to provide reliable data.
2. Age and disease progression significantly affects mechanical properties of the chondral tissue.
3. In combination with biochemical analysis, nanoindentation may provide deeper understating of degenerative processes driving the progression of osteoarthritis.

The common denominator for the works presented is nanotechnology in biomedicine. Both synthesis and analysis at the nanoscale regime require careful design and execution of experimental techniques. Despite many research initiatives devoted to nanotechnology, there is still a missing link between basic science and widespread adoption. Hopefully, my work will further the understanding of nanotechnology and facilitate its broad adoption in biomedicine.

My current research is devoted to the application of nanotechnology in 3D bioprinting, which is an exciting technology allowing for precise layer-by-layer deposition of cells and biomaterials. 3D bioprinting opens an avenue for novel tissue engineering approaches, aiming at tissue reconstruction or regeneration. It may also be utilized for the creation of spatially refined tissue or disease models. The goal of utilizing nanotechnology in 3D bioprinting is to create optimal conditions for cellular growth, proliferation, and differentiation. My yet unpublished results focus on creating polycaprolactone reinforced with carbon nanotubes, which can be utilized as a strengthening scaffold for tissue constructs. Preliminary data indicate that at a particular concentration of carbon nanotubes, cell adhesion is significantly facilitated while maintaining excellent printability.

Regarding VLPs, my current work is focused on utilizing SARS-CoV-2 epitopes for specific binding of anty-SARS-CoV-2 antibodies for immunodiagnostic purposes. As mentioned previously, It has resulted in patent application titled “Hybrid nanoparticles binding antibodies, the method of their production and use for binding specific anti-SARS-CoV-2 antibodies” [**NCA 9]**.

My current involvement in thematically different research projects allows me to continue the exploration of various STEM field related topics, while utilizing and building upon the knowledge I have gathered so far.

7. References

[1] J.W.M. Bulte, Superparamagnetic iron oxides as MPI tracers: A primer and review of early applications, Adv. Drug Deliv. Rev. 138 (2019) 293–301. https://doi.org/10.1016/j.addr.2018.12.007.

[2] L. Xie, W. Jin, H. Chen, Q. Zhang, Superparamagnetic iron oxide nanoparticles for cancer diagnosis and therapy, J. Biomed. Nanotechnol. 15 (2019) 215–235. https://doi.org/10.1166/jbn.2019.2678.

[3] N.S.M. Shahrodin, J. Jaafar, A.R. Rahmat, N. Yusof, M.H. Dzarfan Othman, M.A. Rahman, Superparamagnetic Iron Oxide as Photocatalyst and Adsorbent in Wastewater Treatment – A Review, Micro Nanosyst. 12 (2019) 4–22. https://doi.org/10.2174/1876402911666190716155658.

[4] A. Erwin, S. Salomo, P. Adhy, N. Utari, W. Ayu, Y. Wita, S. Nani, Magnetic iron oxide particles (Fe3O4) fabricated by ball milling for improving the environmental quality, in: IOP Conf. Ser. Mater. Sci. Eng., Institute of Physics Publishing, 2020: p. 012051. https://doi.org/10.1088/1757-899X/845/1/012051.

[5] J.E. Muñoz, J. Cervantes, R. Esparza, G. Rosas, Iron nanoparticles produced by high-energy ball milling, J. Nanoparticle Res. 9 (2007) 945–950. https://doi.org/10.1007/s11051-007-9226-6.

[6] M.M. Can, S. Ozcan, A. Ceylan, T. Firat, Effect of milling time on the synthesis of magnetite nanoparticles by wet milling, Mater. Sci. Eng. B Solid-State Mater. Adv. Technol. 172 (2010) 72–75. https://doi.org/10.1016/j.mseb.2010.04.019.

[7] Y. Zhao, D. Sultan, Y. Liu, Biodistribution, excretion, and toxicity of nanoparticles, in: Theranostic Bionanomaterials, Elsevier, 2019: pp. 27–53. https://doi.org/10.1016/B978-0-12-815341-3.00002-X.

[8] L.C. Varanda, C.G.S. Souza, D.A. Moraes, H.R. Neves, J.B. Souza Junior, M.F. Silva, R.A. Bini, R.F. Albers, T.L. Silva, W. Beck, Size and shape-controlled nanomaterials based on modified polyol and thermal decomposition approaches. A brief review, An. Acad. Bras. Cienc. 91 (2019). https://doi.org/10.1590/0001-3765201920181180.

[9] M.O. Mohsen, L. Zha, G. Cabral-Miranda, M.F. Bachmann, Major findings and recent advances in virus–like particle (VLP)-based vaccines, Semin. Immunol. 34 (2017) 123–132. https://doi.org/10.1016/j.smim.2017.08.014.

[10] H. Garg, T. Mehmetoglu-Gurbuz, A. Joshi, Virus Like Particles (VLP) as multivalent vaccine

candidate against Chikungunya, Japanese Encephalitis, Yellow Fever and Zika Virus, Sci. Rep. 10 (2020) 1–13. https://doi.org/10.1038/s41598-020-61103-1.

[11] G. Saha, P. Saudagar, V.K. Dubey, Virus-like particles: nano-carriers in targeted therapeutics, INC, 2020. https://doi.org/10.1016/b978-0-12-819363-1.00012-0.

[12] J. Fuenmayor, F. Gòdia, L. Cervera, Production of virus-like particles for vaccines, N. Biotechnol. 39 (2017) 174–180. https://doi.org/10.1016/j.nbt.2017.07.010.

[13] M.F. Hagan, Controlling viral capsid assembly with templating, Phys. Rev. E - Stat. Nonlinear, Soft Matter Phys. 77 (2008) 051904. https://doi.org/10.1103/PhysRevE.77.051904.

[14] A.A. Mieloch, M. Kręcisz, J.D. Rybka, A. Strugała, M. Krupiński, A. Urbanowicz, M. Kozak, B. Skalski, M. Figlerowicz, M. Giersig, The influence of ligand charge and length on the assembly of Brome mosaic virus derived virus-like particles with magnetic core, AIP Adv. 8 (2018). https://doi.org/10.1063/1.5011138.

[15] M.R. VanLandingham, Review of instrumented indentation, J. Res. Natl. Inst. Stand. Technol. 108 (2003) 249–265. https://doi.org/10.6028/jres.108.024.

[16] N. Rodriguez-Florez, M.L. Oyen, S.J. Shefelbine, Insight into differences in nanoindentation properties of bone, J. Mech. Behav. Biomed. Mater. 18 (2013) 90–99. https://doi.org/10.1016/j.jmbbm.2012.11.005.

[17] M. Ramezanzadehkoldeh, B. Skallerud, Nanoindentation response of cortical bone: dependency of subsurface voids, Biomech. Model. Mechanobiol. 16 (2017) 1599–1612. https://doi.org/10.1007/s10237-017-0907-5.

[18] N. Shimomura, R. Tanaka, Y. Shibata, Z. Zhang, Q. Li, J. Zhou, Wurihan, T. Tobe, S. Ikeda, K. Yoshikawa, Y. Shimada, T. Miyazaki, Exceptional contact elasticity of human enamel in nanoindentation test, Dent. Mater. 35 (2019) 87–97. https://doi.org/10.1016/j.dental.2018.11.005.

[19] G. Kermani, A. Hemmasizadeh, S. Assari, M. Autieri, K. Darvish, Investigation of inhomogeneous and anisotropic material behavior of porcine thoracic aorta using nano-indentation tests, J. Mech. Behav. Biomed. Mater. 69 (2017) 50–56. https://doi.org/10.1016/j.jmbbm.2016.12.022.

[20] K. Park, G.E. Lonsberry, M. Gearing, A.I. Levey, J.P. Desai, Viscoelastic Properties of Human Autopsy Brain Tissues as Biomarkers for Alzheimer's Diseases, IEEE Trans. Biomed. Eng. 66 (2019) 1705–1713. https://doi.org/10.1109/TBME.2018.2878555.

[21] M. V. Swain, J. Nohava, P. Eberwein, A simple basis for determination of the modulus and hydraulic conductivity of human ocular surface using nano-indentation, Acta Biomater. 50 (2017) 312–321. https://doi.org/10.1016/j.actbio.2016.12.007.

8. Appendix

SCIENTIFIC REPORTS
nature research

OPEN

Bioevaluation of superparamagnetic iron oxide nanoparticles (SPIONs) functionalized with dihexadecyl phosphate (DHP)

Adam Aron Mieloch[1], Magdalena Żurawek[2], Michael Giersig[1,3], Natalia Rozwadowska[2] & Jakub Dalibor Rybka[1*]

Superparamagnetic iron oxide nanoparticles (SPIONs) have been investigated for wide variety of applications. Their unique properties render them highly applicable as MRI contrast agents, in magnetic hyperthermia or targeted drug delivery. SPIONs surface properties affect a whole array of parameters such as: solubility, toxicity, stability, biodistribution etc. Therefore, progress in the field of SPIONs surface functionalization is crucial for further development of therapeutic or diagnostic agents. In this study, SPIONs were synthesized by thermal decomposition of iron (III) acetylacetonate Fe(acac)$_3$ and functionalized with dihexadecyl phosphate (DHP) *via* phase transfer. Bioactivity of the SPION-DHP was assessed on SW1353 and TCam-2 cancer derived cell lines. The following test were conducted: cytotoxicity and proliferation assay, reactive oxygen species (ROS) assay, SPIONs uptake (*via* Iron Staining and ICP-MS), expression analysis of the following genes: alkaline phosphatase (*ALPL*); ferritin light chain (*FTL*); serine/threonine protein phosphatase 2A (*PP2A*); protein tyrosine phosphatase non-receptor type 11 (*PTPN11*); transferrin receptor 1 (*TFRC*) *via* RT-qPCR. SPION-DHP nanoparticles were successfully obtained and did not reveal significant cytotoxicity in the range of tested concentrations. ROS generation was elevated, however not correlated with the concentrations. Gene expression profile was slightly altered only in SW1353 cells.

Utilization of superparamagnetic iron oxide naoparticles (SPIONs) spans from diagnostics, imaging and magnetic separation to targeted drug delivery and magnetic hyperthermia[1–4]. This chemically inert and biocompatible material provides a great platform for biomedical applications. The polydispersity level is a crucial factor affecting many properties of SPIONs such as e.g. magnetic properties, biodistribution, cytotoxicity[5]. The most robust methods of SPIONs synthesis, providing highly monodisperse particles at large quantities, rely on thermal decomposition of organic salts. The drawback of these methods is the need to utilize surfactants during the synthesis, which are indispensable for a proper particle formation. Consequently, the surface of as-obtained SPIONs is covered with hydrophobic moieties and requires subsequent functionalization. This step does not only provide hydrophilic properties, necessary for many biological applications, but also allows for fine tuning of such properties as e.g. surface charge, hydrodynamic radius, colloidal stability etc. which in turn affect their overall performance. Numerous studies have demonstrated different types of ligands used for iron oxide nanoparticles` functionalization. Some of them include: poly(ethylene glycol)(PEG), poly(vinyl pyrrolidone)(PVP), poly(vinyl alcohol) (PVA), poly(lactic-co-glycolic acid) (PLGA), dextran, gelatin, starch, alginate, chitosan, albumin, casein, polydopamine, dendrimers and many more[6–17]. However, there is scarcity of data regarding functionalization exposing phosphate group. From the standpoint of bioactivity and biodistribution, physicochemical properties of nanoparticles play a crucial role in protein corona formation. Upon exposition to biological fluids,

[1]Center for Advanced Technology, Adam Mickiewicz University in Poznan, Uniwersytetu Poznańskiego 10, 61-614, Poznan, Poland. [2]Institute of Human Genetics, Polish Academy of Sciences, Strzeszynska 32, 60-470, Poznan, Poland. [3]Department of Physics, Institute of Experimental Physics, Freie Universität, Arnimallee 14, 14195, Berlin, Germany. *email: jrybka@amu.edu.pl

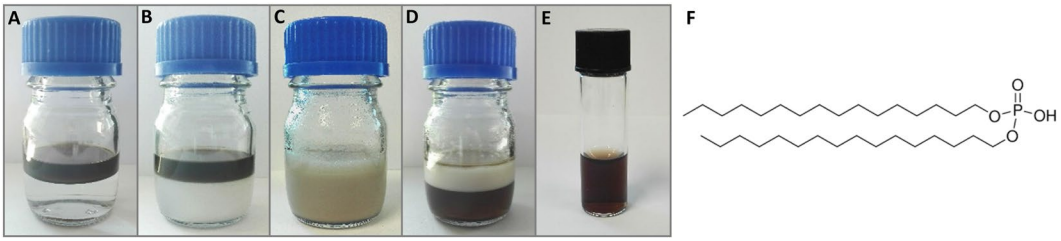

Figure 1. Steps of SPIONs functionalization with DHP. (**A**) Upper phase: hexane, DHP, iron oxide nanoparticles. Lower phase: water. (**B**) Solution after phase transfer of DHP from hexane to water. (**C**) Solution after functionalization. (**D**) 12 h after functionalization. (**E**) Functionalized iron oxide nanoparticles after purification. (**F**) molecular structure of dihexadecyl phosphate (DHP).

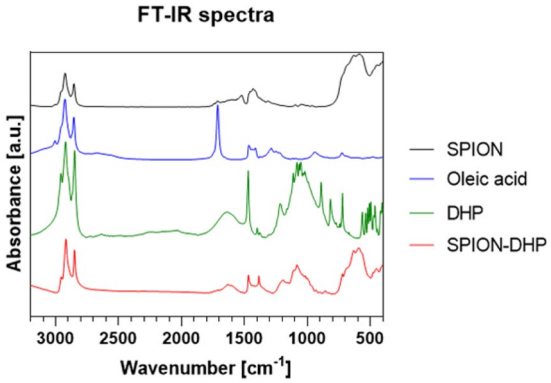

Figure 2. Fourier Transform Infrared Spectroscopy analysis.

such parameters as e.g. size, surface curvature, surface charge, hydrodynamic diameter or functional groups, govern the affinity of certain proteins to the nanoparticles' surface[18]. Moreover, differences in the protein corona composition have been demonstrated to correlate with SPIONs biodistribution *in vivo*[19]. The aim of this study is to provide a detailed protocol for SPIONs functionalization with dihexadecyl phosphate (DHP) and broad biological assessment of its interactions with human cells. The following biological analyses of the SPION-DHP were performed: proliferation/viability assay, iron content measurements, reactive oxygen species (ROS) generation, gene expression profile including: alkaline phosphatase (ALPL); ferritin light chain (FTL); serine/threonine protein phosphatase 2A (PP2A); protein tyrosine phosphatase non-receptor type 11 (PTPN11); transferrin receptor 1 (TFRC).

Results

Dihexadecyl (DHP) functionalization. The surface of as synthesized nanoparticles is covered in oleic acid residues, with hydrophobic chain directed outward, into the solution. To obtain solubility in water, 15.6 ± 0.9 nm superparamagnetic iron oxide nanoparticles (Fig. S1) were functionalized with DHP surfactant, containing two hydrophobic chains and hydrophilic phosphate group. Functionalization is achieved through hydrophobic interactions of DHP and oleic acid alkyl chains. In the first step, DHP is dissolved in hexane and mixed with chloroform solution of iron oxide nanoparticles (Fig. 1A). In the next step, water is added and the solution is mixed until water phase becomes turbid. This stage of DHP phase transfer from hexane to water was crucial to successful functionalization (Fig. 1B). Post synthesis, solution was uniformly light brown with layer of foam at the top (Fig. 1C). 12 h incubation after synthesis allows for phase separation and removal of the unbound DHP located at the boundary between water and hexane and partially dispersed in hexane (Fig. 1D). After magnetic separation and filtration, sample was redispersed in water and subjected to analyses (Fig. 1E). In order to confirm that the functionalization was successful, FT-IR analysis was performed (Fig. 2). The concentration of SPION-DHP was measured with TGA, described in material and methods. In our previous studies, hydrodynamic radius (*via* dynamic light scattering – DLS) and ζ-potential of DHP coated SPIONs was assessed[20]. In the study: ζ-potential $= -44.0 \pm 3.4$ mV and hydrodynamic diameter $= 53.75 \pm 1.93$ nm.

FT-IR analysis confirmed the presence of DHP on the surface of SPIONs. SPION-DHP clearly shows band patterns corresponding to all constituents (Table 1). Bands at 3000–2800 cm^{-1} relate to CH_2 and CH_3 groups of oleic acid and DHP. The signal between 1700–1600 cm^{-1} stems from O=P-H group characteristic for DHP. The wide peak at 1415–1085 cm^{-1} is the most prominent signal derived from P=O groups[21,22]. The signal at around 600 cm^{-1} corresponds to Fe-O bonds[23].

Absorption [cm^{-1}]	Group
3000–2800	CH_2, CH_3
1760	C=O, carboxylic acid
1690	C=C, isolated
1740–1600	O=P-OH
1415–1085	P=O
1260–1000	C-O
1040–909	P-O
600	Fe-O

Table 1. Fourier Transform Infrared Spectroscopy spectra characterization.

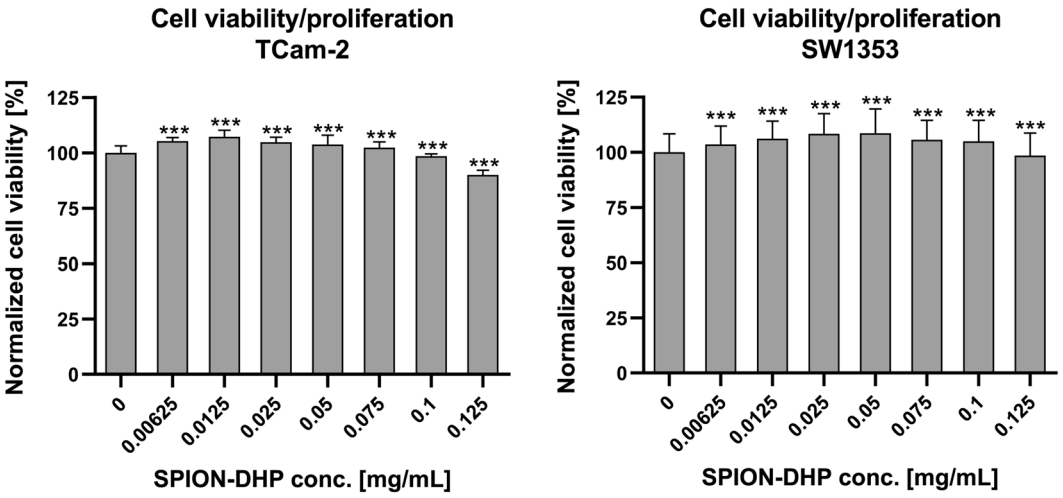

Figure 3. CellTiter-Glo 2.0 assay. One-way ANOVA statistical analysis was used to calculate the significance of the data, $\alpha = 0.05$. 24 h after seeding, SPION-DHP at different concentrations were added and incubated for 24 h. Asterisks indicate statistically significant differences in comparison to control group (***$P \leq 0.05$).

Viability/proliferation analysis. Cell viability/proliferation assay indicates very low cytotoxicity in the range of tested concentration (Fig. 3). At the highest concentration of SPION-DHP (0.125 mg/mL) the viability of TCam-2 was 90 ± 2%; SW1353 98 ± 10%, normalized for the cells without nanoparticles.

Iron staining. Prussian blue-based staining was performed to assess the cellular internalization of SPION-DHP. However, no staining was detected for both cell types. For comparison, SPION-DMSA nanoparticles were administered ($\zeta = -49{,}3$ mV[24]). In this case, blue stain was observed, indicating internalization of the nanoparticles (Fig. 4). In order to establish if DHP coated nanoparticles were not internalized or if they can't be detected with Prussian blue staining, 0.1 mg/mL of both SPION-DHP and SPION-DMSA were suspended in PBS, and subjected to the reaction (Fig. 5). No reaction was detected for SPION-DHP, indicating Prussian blue staining incompatible for the assessment of cellular iron concentration for DHP funcionalized SPIONs. To confirm the internalization of SPION-DHP, Inductively Coupled Plasma Mass Spectrometry (ICP-MS) analysis was performed instead (Fig. 6). The method was developed and described in our previous study[24]. For TCam-2 cells, the highest intracellular iron concentration (316 ± 18 ppb) was detected at 0.025 mg/mL of SPION-DHP. For SW1353, the highest concentration (215 ± 15 ppb) of intracellular iron was detected for the highest concentration of SPION-DHP, 0.1 mg/mL.

ICP-MS iron concentration analysis. *Reactive oxygen species (ROS) generation.* ROS generation was assessed using fluorogenic probes DCFDA/H2DCFDA (Fig. 7). Although slight, statistically significant increase was observed for both TCam-2 and SW1353 after SPION-DHP administration, it was not correlated with the increase of concentration.

Gene expression analysis. The following genes where selected for gene expression analysis: transferrin receptor 1 (TFRC); ferritin light chain (FTL); alkaline phosphatase (ALPL); serine/threonine protein phosphatase 2A (PP2A); protein tyrosine phosphatase non-receptor type 11 (PTPN11).

Transferrin receptor (TFRC; CD71). Iron metabolism is crucial for various biochemical processes, providing normal functioning of cells and organs of the human body. Due to its involvement is such processes as e.g. the formation of heme- and iron-containing proteins participating in oxygen transport, energy metabolism, DNA synthesis etc., it requires precise control over its intracellular concentration[25,26]. Transferrin receptor is a membrane

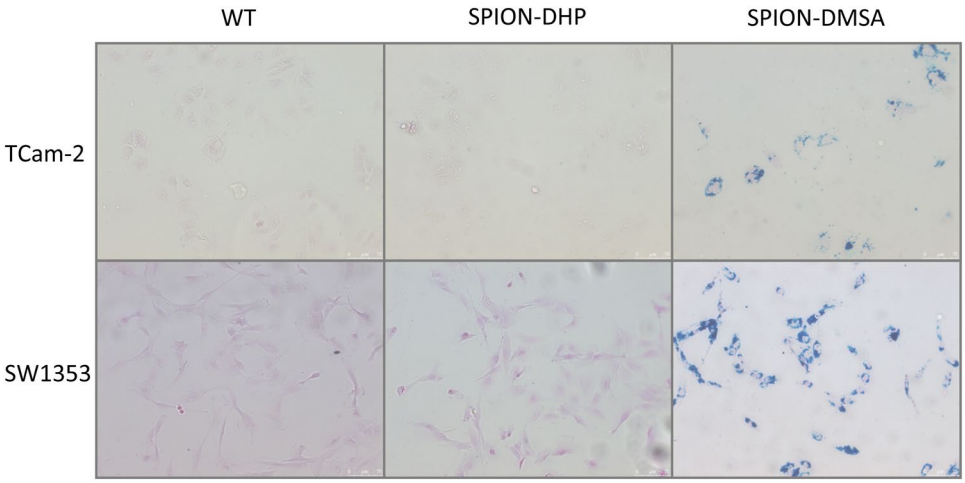

Figure 4. Prussian blue staining was performed for quantitative evaluation of the SPIONs uptake using the Iron Staining Kit (Sigma Aldrich, MO, USA). TCam-2 and SW1353cells were seeded at density of 50,000 and 100,000 cells (respectively) per well on 12-well plate. After 24 h incubation the SPION-DHP and SPION-DMSA were applied to cells in complete growth medium to final concentration of 0.1 mg/mL. Prussian blue staining was performed 24 h after iron oxide nanoparticles administration.

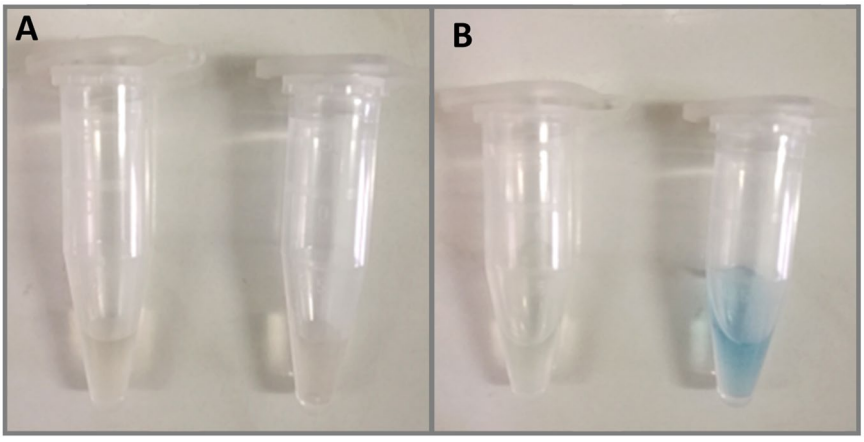

Figure 5. SPION-DHP and SPION-DMSA in Prussian blue reaction. (**A**) SPION-DHP (left) and SPION-DMSA (right) at 0.1 mg/mL concentration in PBS. (**B**) SPION-DHP (left) and SPION-DMSA (right) after 10 minutes incubation in Potassium Ferrocyanide and Hydrochloric Acid Solution (IRON STAIN Solution, Sigma Aldrich, MO, USA). Ionic iron of DMSA-NP reacted with acid ferrocyanide producing a blue color.

glycoprotein, which can import iron by binding a plasma glycoprotein, transferrin (TF). TF is the serum protein with two specific Fe^{3+}-binding sites.

At the pH = 7.4, TFRC binds iron-bearing TF, either monoferric or diferric. Subsequently, TF/TFRC assembly is internalized and transferred to endosome, where at the pH = 5.6, iron ions are released[27]. TFRC gene was chosen to investigate if there is a biologically significant iron ions leakage from SPIONs present in cell culture.

Ferritin is an intracellular protein, governing the storage and release of iron ions. Under aerobic conditions, ferritin promotes oxidation of the Fe(III) ions, which are subsequently stored in a form of aggregates. Human ferritin is composed of two subunit types: light chains and heavy chains. The expression of ferritin light chain (FTL) is strictly related to bioavailability of Fe(II) ions[28]. This gene was chosen due to reported increase of ferritin expression after iron oxide nanoparticles administration, which is caused by their gradual degradation, followed by the increased availability of iron ions[29,30].

Alkaline Phosphatase (ALP; EC: 3.1.3.1) is an abundant glycoprotein bound to the cellular membranes, acting as a potent catalyst of phosphate monoesters hydrolysis at basic pH. The alkaline phosphatases (ALPs) of mammals belong to the category of metalloenzymes. ALPs active site contains two Zn^{2+} and one Mg^{2+} ions, required for enzymatic activity[31]. This gene was chosen on the assumption of interaction between phosphate group from DHP and alkaline phosphate. Despite DHP being phosphate diester, its intracellular hydrolysis could potentially provide the substrate for enzymatic reaction. ALP is encoded by the ALPL gene.

31

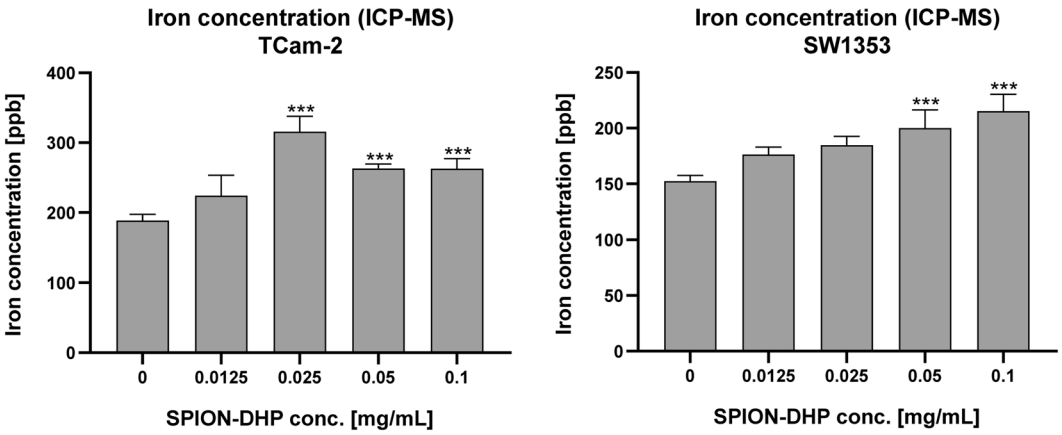

Figure 6. Inductively Coupled Plasma Mass Spectrometry (ICP-MS) analysis. One-way ANOVA statistical analysis was used to calculate the significance of the data, $\alpha = 0.05$. 24 h after seeding, SPION-DHP at different concentrations were added and incubated for 24 h. Asterisks indicate statistically significant differences in comparison to control group (***$P \leq 0.05$).

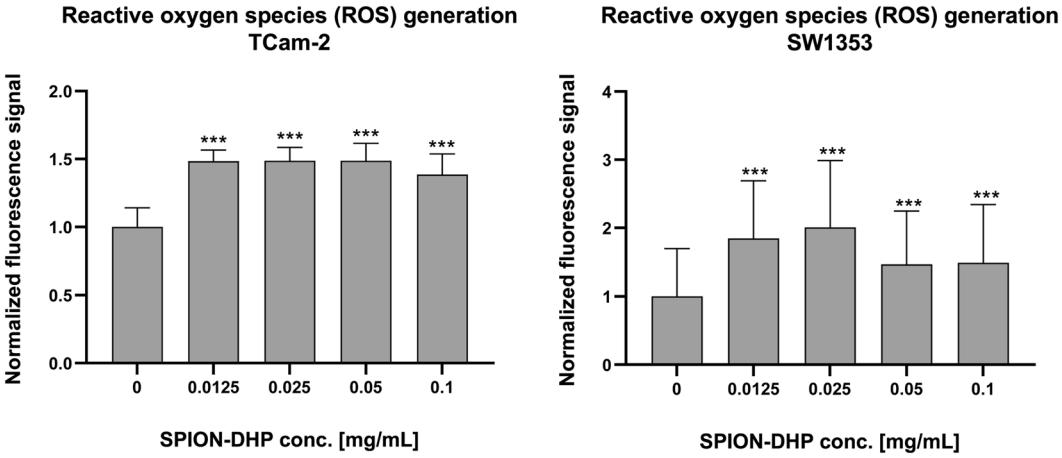

Figure 7. Reactive Oxygen Species (ROS) test. ROS production in SPION-DHP treated cells was investigated using fluorogenic probes DCFDA/H2DCFDA - Cellular ROS Assay Kit One-way ANOVA statistical analysis was used to calculate the significance of the data, $\alpha = 0.05$. 24 h after seeding, SPION-DHP at different concentrations were added and incubated for 24 h. Asterisks indicate statistically significant differences in comparison to control group (***$P \leq 0.05$).

Protein Phosphatase 2A (PP2A; EC: 3.1.3.16) is a crucial and widely expressed serine threonine phosphatase, responsible for the regulation of many cellular processes through the mechanism of dephosphorylation[32]. PP2A is crucial in such processes as e.g.: signal transduction, glycolysis, lipid metabolism, DNA replication, cell proliferation, transcription and translation, cell mobility and apoptosis[33]. Natively, protein phosphatases nucleophilically attack and dephosphorylate three types of amino acids: tyrosine (Tyr), threonine (Thr) and serine (Ser)[34]. This gene was chosen to establish whether DHP can be a potential target for PP2A catalytic activity.

Protein Tyrosine Phosphatase non-receptor Type 11 (PTPN11; EC 3.1.3.48). The product of PTPN11 gene, Src homology region 2 domain-containing phosphatase-2 (SHP-2), is ubiquitously expressed among tissues. SHP2 regulates both physiological and pathological processes including cell survival, migration and proliferation through the positive (signal-enhancing) and/or negative (signal-inhibiting) regulation of signaling pathways. The main SHP2 signaling routes involve phosphatidylinositol 3-kinase (PI3K)-AKT, Ras-Raf-mitogen-activated kinase (MAPK) and Janus tyrosine kinase (JAK)/signal transducer and activator of transcription (STAT) in response to cytokine, hormonal, and growth factor stimulation or genomic damage in a cell-specific manner[35,36]. This gene was chosen to assess if DHP covered SPION can act as a substrate for SHP2 enzymatic activity.

TCam-2. *SW1353.* No statistically significant changes in all tested genes were observed after administration of 0.1 mg/mL SPION-DHP to TCam-2 cells (Fig. 8). Statistically significant changes in gene expression were observed for ALPL, FTL and PTPN11 in SW1353 cells (Fig. 9).

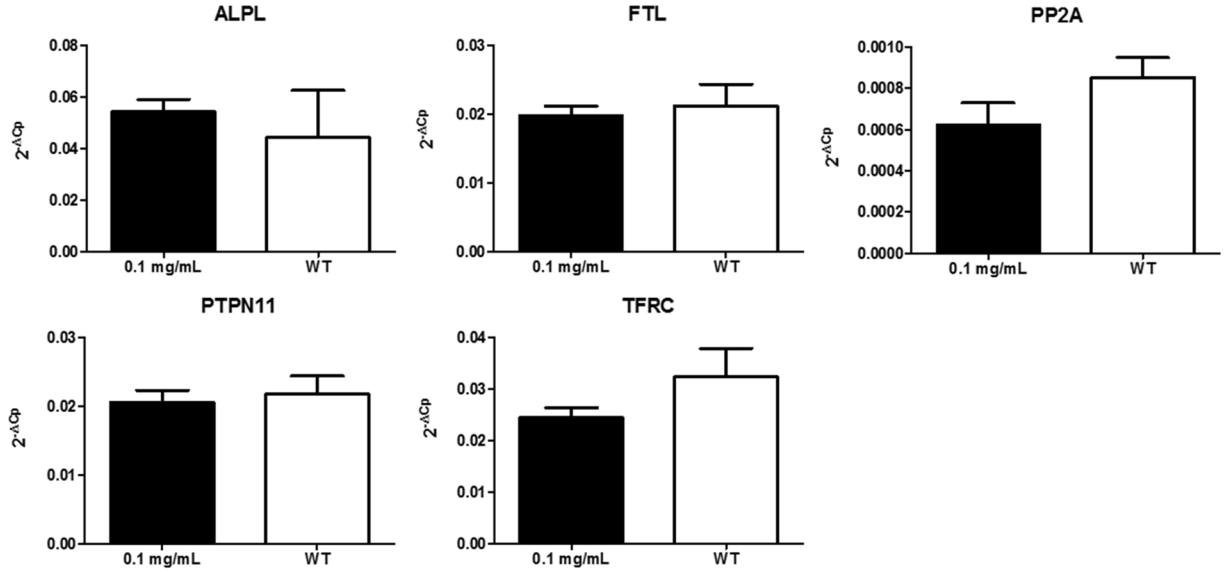

Figure 8. Expression analysis of selected genes in TCam-2 cells treated with SPIONs and wild type. Relative expression level was calculated using the $2-\Delta Cp$ formula. The data are presented as mean relative expression level ± SD. TCam-2 cells were treated with 0.1 mg/mL SPIONs; WT- wild type, non-labeled cells; ALPL- alkaline phosphatase; FTL- ferritin light chain; PP2A-serine/threonine protein phosphatase 2A; PTPN11- protein tyrosine phosphatase, non-receptor type 11; TFRC- transferrin receptor 1.

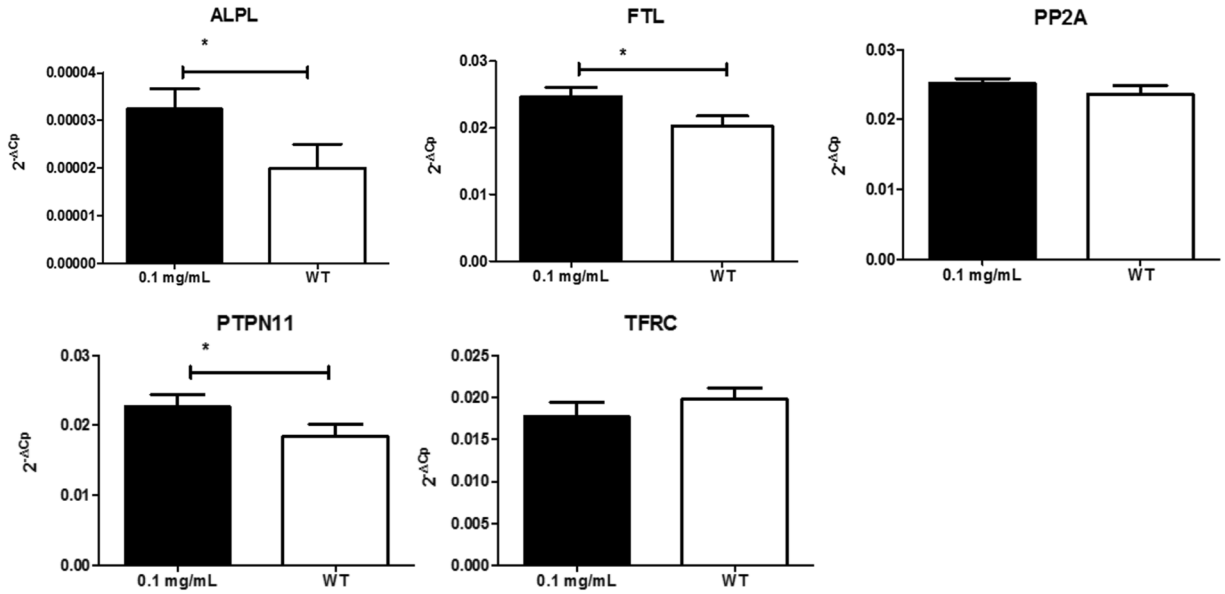

Figure 9. Expression analysis of selected genes in SW1353 cells treated with SPIONs and wild type. Relative expression level was calculated using the $2-\Delta Cp$ formula. The data are presented as mean relative expression level ± SD. Asterisk indicate statistical significance ($*P < 0.05$). SW1353 cells were treated with 0.1 mg/mL SPIONs; WT- wild type, non-labeled cells; ALPL- alkaline phosphatase; FTL- ferritin light chain, PP2A-serine/threonine protein phosphatase 2A; PTPN11- protein tyrosine phosphatase, non-receptor type 11; TFRC- transferrin receptor 1.

Discussion

The functionalization of SPIONs with DHP is a straightforward process, yielding a stable colloidal suspension of SPION-DHP nanoparticles. In our previous studies, these particles were successfully used to create virus-like particles with magnetic cores[20,37]. Viability/proliferation assay revealed very low toxicity up to 0.125 mg/mL concentration for TCam-2 and SW1353 cells (Fig. 3). Iron concentration assay *via* Prussian blue staining revealed that SPION-DHP nanoparticles are resistant to the staining and cannot be detected with this method (Figs. 4 and 5). In comparison, SPION-DMSA nanoparticles were easily recognized with this method. The exact mechanism underlying resistance of SPION-DHP staining against Prussian blue has not been identified. Presumably,

33

DHP coating prevents SPIONs from being dissolved with HCl, which results in lack of iron ions required for Prussian blue reaction. To assess the internalization of SPION-DHP *via* intracellular iron concentration measurement, ICP-MS was used (Fig. 6). In both cases, intracellular iron concentration increased after SPION-DHP administration. For TCam-2, statistically significant increase was observed for all concentrations at maximum of 316 ± 18 ppb for 0.025 mg/mL (188 ± 7 ppb for control). For SW1353, statistically significant increase was observed for 0.05 mg/mL (200 ± 16 ppb) and 0.1 mg/mL (215 ± 15 ppb), in comparison to control (152 ± 5 ppb). This data indicates, that SPION-DHP were successfully internalized by both cell types. Non-linear increase in intracellular iron concentration in TCam-2 cells could be explained if SPION-DHP internalization occurs by receptor-mediated endocytosis. In this case, receptor depletion would inhibit further internalization of the nanoparticles. It has been demonstrated that SPIONs can be internalized by several endocytic uptake pathways, such as phagocytosis, caveolae-dependent endocytosis, clathrin-dependent endocytosis or macropinocytosis[38]. Therefore, cell-type dependent efficiency in SPION-DHP internalization could be assumed. Iron oxide nanoparticles have been shown to facilitate redox reactions (as the reactant or catalyst) resulting in generation of reactive oxygen species. Iron species participate in homogenous Fenton, Fenton-like and Haber-Weiss reactions. Products of these reactions such as superoxide radicals, hydroxyl radicals, or ferryl-oxo complexes are highly reactive in cellular environment, and are capable of exerting severe cellular damage. Additionally, it has been demonstrated that iron oxides can initiate heterogeneous redox reactions at the water/solid interfaces, increasing the probability of ROS-related toxicity[39,40]. Although elevated ROS levels were detected after administration of SPION-DHP to TCam-2 and SW1353 cells, they were not dependent on the concentrations administered (Fig. 7). The observed increase in ROS generation did not have a negative impact on short-term proliferation/viability of the cells. Gene expression analysis revealed discrepancies between cell lines (Figs. 8 and 9). There were no statistically significant changes in gene expression for all genes tested, after administration of 0.1 mg/mL SPOION-DHP in TCam-2 cells. The same concentration elicited increased expression of ALPL, FTL and PTPN11 genes in SW1353 cells. The lack of increase in transferrin receptor suggests that the nanoparticles in culture medium remained intact and did not release significant amounts of iron ions. Slight increase in transferrin light chain expression was observed in SW1353 cells. This may indicate a partial release of iron ions from SPION-DHP nanoparticles. Alkaline phosphatase expression in SW1353 was significantly elevated. However, the lack of the increase in TCam-2 cells indicates that the elevated expression was not a result of DHP hydrolysis, providing substrate for the enzymatic reaction, but rather a complex response for SPION-DHP administration. Protein Tyrosine Phosphatase non-receptor Type 11 expression was also slightly increased in case of SW1353 cells. Similarly to ALP, its involvement in many cellular processes suggests a complex cellular response to the nanoparticles administration rather than a direct interaction with their surface or disintegration products. Biological evaluation of DHP coated SPIONs indicates their low, however cell-type dependent cytotoxicity. TCam-2 cells appeared as more resilient in comparison to SW1353 cells. In regard to protein corona formation, existing studies suggest that upon exposition to biological fluids SPION-DHP nanoparticles would display affinity mainly for albumin and retain its negative surface charge. It has been demonstrated, that regardless of the zeta potential (positive, neutral, negative), polyvinyl acid- or dextran-coated SPIONs, showed negative zeta potential after exposition to PBS + serum solution[41]. However, to elucidate effects of DHP coating on protein corona formation, further studies are required.

Summary. This study presents a ready-to-use protocol for iron oxide nanoparticles functionalization with dihexadecyl phosphate. SPION-DHP nanoparticles did not reveal significant cytotoxicity in the range of tested concentrations. ROS generation was elevated, however not correlated to the concentrations. Gene expression profile was slightly altered only in SW1353 cells. In summary, this preliminary investigation indicates that SPION-DHP hold a great potential for biological applications.

Materials and Methods

Materials. Oleic acid (technical grade 90%), Iron (III) acetylacetonate (97%), Dihexadecyl phosphate, 1-octadecene (90%), 2-butanol (95,5%), Sodium dodecyl sulfate (99%), Paraformaldehyde (95%) were purchased from Sigma-Aldrich (Sigma-Aldrich, MO, USA). Toluene (99,5%), n-Hexane (99%) and Chloroform (98,5%) were purchased from Avantor (Avantor, Gliwice, Poland) were used as received. Water was purified by Hydrolab HLP5 instrument (0.09 µS/cm).

Synthesis of superparamagnetic iron oxide nanoparticles (SPIONs). Spherical iron oxide nanoparticles were synthesized via thermal decomposition of iron (III)acetylacetonate $Fe(acac)_3$. This method has been described in our previous works[20,42] Briefly, 6 mmol of $Fe(acac)_3$ and 18 mmol of oleic acid were dissolved in 40 mL of 1-octadecene. The reaction was performed with continuous stirring and nitrogen flow. Temperature of the solution was increased to 220 °C and maintained for 1 h. Subsequently, the temperature was increased further to 320 °C and maintained for 1 h. After the synthesis, the solution was left to cool down to ambient temperature and 200 mL of washing solution (3:1 v/v of 2-butanol and toluene) was added. The obtained mixture was placed on a neodymium magnet and left overnight to allow nanoparticles to precipitate. Supernatant was discarded and replaced with fresh washing solution. Sonicating bath was used to resuspend nanoparticles. The washing step was performed thrice. In the final step, nanoparticles were suspended in 20 mL of chloroform. Concentration of the nanoparticles was estimated by dried sample weighing. Size of the particles was analyzed using ImageJ 1.8 Software. 100 particles were analyzed. Mean diameter = 15.6 ± 0.9 nm.

Transmission electron microscopy (TEM). 10 µl of sample was placed on carbon coated copper grid. The excess was removed with blotting paper. Sample was visualized with Hitachi TEM HT7700 microscope. Images were analyzed with ImageJ software.

Functionalization with dihexadecyl phosphate (DHP). DHP functionalization was performed in accordance to our previously described method[20,42]. 10.0 mg of dihexadecyl phosphate were added to 20 mL of hexane and dissolved with heat-assisted magnetic stirring (75 °C, ca. 10 min). After DHP dissolution, a chloroform solution containing 10.0 mg of synthesized iron oxide nanoparticles coated with oleic acid was added. The mixture was shortly sonicated and 80 mL of water were added. Subsequently, the obtained two-phase solution was briefly vortexed and sonicated until the water phase became turbid. In the next step, the solution was placed in a sonicating bath for 3–4 h with no temperature control. After the functionalization, the solution was left overnight to allow for phase separation. The bottom phase was collected and placed near neodymium magnet for 24 h to separate functionalized nanoparticles from the solution. The obtained precipitate was collected, suspended in 2 mL of miliQ water and filtered through 0.22 μm pores. Concentration of the SPION-DHP nanoparticles was measured *via* thermogravimetric analysis described below.

Functionalization with meso-2,3-dimercaptosuccinic acid (DMSA). Ligand exchange procedure was performed to exchange the capping ligand from oleic acid to meso-2,3-dimercaptosuccinic acid (DMSA). This method has been described in our previous work[24]. In the first step, 50 mg of DMSA was dissolved in 15 mL dimethylsulfoxide (DMSO) and 100 mg of nanoparticles were diluted in 15 mL of chloroform. Solutions were mixed together and 50 μL of triethylamine was added as the catalyst. Reaction was carried out at 60 °C for 6 hours (shaken vigorously) in a horizontal shaker. Nanoparticles were washed with ethanol, collected with neodymium magnet. The procedure was repeated until the supernatant was transparent, and eventually nanoparticles were resuspended in 20 mL of ethanol. Then, the second step of reaction was carried out. Obtained solution was mixed with 50 mg of DMSA dissolved in 15 mL of DMSO and 50 μL of triethylamine was added. The reaction conditions were the same as in the first step. Washing procedure was also similar, except that ultrapure water was used instead of ethanol. Finally, nanoparticles were resuspended in 10 mL of ultrapure water. For the use in *in vitro* tests, particles were sterile filtered with cellulose acetate syringe filters of two sizes: 0.45 μm and 0.2 μm, respectively.

Fourier-transform infrared spectroscopy (FT-IR). The analysis was performed on Bruker FT-IR IFS 66/s spectrometer. The samples were formed into KBr tablets and analyzed in the 4000–400 cm^{-1} range.

Concentration measurement *via* thermogravimetric analysis (TGA). Thermogravimetric analysis was performed to measure concentrations of the functionalized SPIONs. This method was performed in accordance to our, previously established, protocol[20] The analysis was performed on TGA 4000 System (Perkin Elmer apparatus, Waltham, MA, USA). Briefly, a 20 μL sample was taken for measurement. Each sample was measured in triplicate. The sample was heated from 20 to 150 °C at 10 °C/min in nitrogen atmosphere. The lowest mass was taken as fully dried sample and used for further calculations (Fig. S2). The obtained mass was normalized for 20 mg of the initial sample mass. The mean of three measurements was calculated. Density was derived from weighing 5×15 μL of the sample and dividing the mean mass by volume.

Cell culture. SW1353 cells (ATCC® HTB-94™) were cultured in DMEM F12 with Lf-glutamine medium (Lonza, Switzerland), 10% FBS (Sigma Aldrich, MO, USA) and 1% penicillin-streptomycin-amphotericin B (Lonza, Switzerland). TCam-2 cells (kindly gifted from Dr Riko Kitazawa, Department of Diagnostic Pathology, Ehime University Hospital, Matsuyama, Japan) were cultured in RPMI 1640 GlutaMax medium (Gibco, Thermo Fisher Scientific, MA, USA), 10% HyClone FBS (GE Healthcare, IL, USA) and 1% penicillin-streptomycin-amphotericin B (Lonza, Switzerland). All *in vitro* cultures were carried out at 37 °C and 5% CO_2.

Inductively coupled plasma mass spectrometry (ICP-MS) analysis. ICP-MS was applied for quantitative determination of superparamagnetic iron oxide nanoparticles (SPIONs) uptake. The analysis was performed on the NexION 300D ICP-MS, Perkin Elmer. SW1353 and TCam-2 cells were seeded at density $6 \times 10^4/cm^2$ and $2 \times 10^4/cm^2$, respectively and cultured for 24 h. Next, the SPIONs were added in culture media to final concentration of 0.1 mg/mL, 0.05 mg/mL, 0.025 mg/mL and 0.0125 mg/mL. The untreated cells were indicated as a control. After 24 h incubation SW1353 and TCam-2 cells (4×10^5 cells) were collected, washed twice with PBS and cell pellets were frozen at −80 °C. Before the analysis, cells were thawed and lysed in 100 μL of 10% SDS. Then, the cell lysates were frozen for 24 h, thawed and placed in sonicating bath for 1 h. 25 μL of cell lysates (1×10^5 cells) were dissolved in 125 μL of 65% nitric acid and shaken at 80 °C for 2 h to remove organic compounds. As-prepared samples were diluted 10 folds in DI water and taken for the measurement. Iron content was determined based on the standard curve prepared with a multi element standard solution for ICP-MS in the 1, 10, 100, 1000 ppb range.

SPIONs cellular uptake labeling. Prussian blue staining was performed for quantitative evaluation the SPIONs uptake using the Iron Staining Kit (Sigma Aldrich, MO, USA). SW1353 and TCam-2 cells were seeding at density of $1 \times 10^5$and 5×10^4 cells (respectively) per well on 12-well plate containing microscope cover glasses. After 24 h incubation the SPION-DHP and SPION-DMSA were applied to cells in complete growth medium to final concentration 0.1 mg/mL, 4 wells per group (respectively). SW1353 and TCam-2 cells with no SPIONs added were used as a control. Prussian blue staining was performed 24 h after iron oxide nanoparticles administration. Cells were washed with PBS and fixed with 4% paraformaldehyde solution in PBS. Subsequently, Prussian blue staining was performed according to the manufacturer's protocol. In the last step, the cover glasses were mounted onto slide glasses with gelatin solution. SW1353 and TCam-2 cells were visualized with Leica DMi8 microscope.

Gene	Primer	Sequence	Amplicon size (bp)	Reference
ACTB	Forward	CTTCCTGGGCATGGAGTCC	112	Designed
	Reverse	ATCTTGATCTTCATTGTGCTG		
ALPL	Forward	GCTCCAGGGATAAAGCAGGT	122	UCSC Genome Browser
	Reverse	CGCCAGTACTTGGGGTCTTT		
FTL	Forward	CAGCCTGGTCAATTTGTACCT	114	Primer Bank
	Reverse	GCCAATTCGCGGAAGAAGTG		
PP2A	Forward	TTGGTGTCTAGAGCTCACCAGC	125	UCSC Genome Browser
	Reverse	TCCATGATTGCAGCTTGGTT		
PTPN11	Forward	CTGGTGTGGAGGCAGAAAAC	125	UCSC Genome Browser
	Reverse	GTGGGTGACAGCTCCATTTC		
TFRC	Forward	ACCATTGTCATATACCCGGTTCA	219	Primer Bank
	Reverse	CAATAGCCCAAGTAGCCAATCAT		

Table 2. Primer sequences used in RT-qPCR.

Proliferation and cytotoxicity assay. To determine the cytotoxicity of SPIONs and their impact on cells proliferation the CellTiter-Glo 2.0 assay (Promega, WI, USA) was performed according to the manufacturer's protocol. TCam-2 cells were seeded at density of 2×10^4 cells per well on 96-well microplate (Falcon white/clear bottom plate, Corning, NY, USA), 8 wells per group. After 24 h of culture the SPIONs were applied to cells in growth medium to final concentration 0.125 mg/mL, 0.1 mg/mL, 0.075 mg/mL, 0.05 mg/mL, 0.025 mg/mL, 0.0125 mg/mL and 0.00625 mg/mL. Potential cytotoxicity of SPIONs was tested after 24 h of incubation. CellTiter-Glo Reagent was added in an equal volume (100 µl) to each well. The luminescence was recorded using Tecan Infinite M200 Pro. The SPIONs untreated cells were indicated as a control. Furthermore, the background luminescence was determined in wells containing medium without cells.

Gene expression analysis. Expression analysis of alkaline phosphatase (*ALPL*); ferritin light chain (*FTL*); serine/threonine protein phosphatase 2 A (*PP2A*); protein tyrosine phosphatase non-receptor type 11 (*PTPN11*); transferrin receptor 1 (*TFRC*) genes was evaluated by quantitative reverse-transcription PCR (RT-qPCR). Total RNA from wild type and 0.1 mg/mL SPIONs treated SW1353 and TCam-2 cells was isolated using RNeasy Mini kit (Qiagen, Hilden, Germany) according to the manufacturer's protocol. The quality and quantity of RNA was estimated by spectrophotometric measurements (NanoDrop ND1000, Thermo Scientific, MA, USA) and 1% agarose gel electrophoresis. 500 ng of RNA was used in RT reaction performed with QuantiTect Reverse Transcription kit (Qiagen, Hilden, Germany). qPCR was evaluated using 2 µl of diluted 1:10 cDNA samples, 1x Hot FIREPol EvaGreen qPCR Mix (Solis, BioDyne, Tartu, Estonia) and 150 nM forward, reverse primers in a total volume of 20 µl. The primer sequences were obtained from the University of California Santa Cruz Genome Browser on Human Genome hg19 assembly (https://genome.ucsc.edu/), Primer Bank (https://pga.mgh.harvard.edu/primerbank/) or were designed (Table 2). PCR reactions were run on BioRad CFX96 Real Time PCR instrument (BioRad Laboratories, CA, USA). The thermal cycling conditions were an initial polymerase activation at 92 °C for 12 minutes, followed by 40 cycles of denaturation at 95 °C for 15 seconds, annealing at 60 °C for 20 seconds and extension at 72 °C for 20 seconds. The melt curve protocol followed with 15 seconds at 95 °C and then 5 seconds each at 0.5 °C increment from 65 °C to 95 °C. The gene expression analysis was evaluated in three experiments. All reactions were run in triplicate. Gene expression data were normalized to ACTB (β-actin) housekeeping gene. Mean cycle threshold (Ct) values were estimated with BioRad CFX Manager 3.1 software. Relative expression levels were calculated using the $2-\Delta Ct$ formula.

Reactive oxygen species (ROS) test. ROS production in SPIONs treated cells was investigated using fluorogenic probes DCFDA/H2DCFDA - Cellular ROS Assay Kit (Abcam, UK), according to the manufacturer's protocol. TCam-2 and SW1353 were seeded at density of 2×10^4 cells and 3×10^4 (respectively) per well on 96-well microplate (Falcon white/clear bottom plate, Corning, NY, USA), 8 wells per group. After 24 h incubation, the SPIONs were applied to cells in the complete growth medium to final concentration 0.1 mg/mL, 0.05 mg/mL, 0.025 mg/mL and 0.0125 mg/mL. SW1353 and TCam-2 cells were treated with SPIONs and incubated for 24 h. Subsequently, cells were washed with 1X buffer and stained with 100 µl of 25 µM DCFDA in 1X Buffer for 45 min. at 37 °C. After the incubation, cells were washed with 1X Buffer. The fluorescence was measured using Tecan Infinite M200 Pro microplate reader at excitation/emission = 485/535 nm, multiple reads per well (3×3 matrix), in a fluorescence top reading mode.

Statistical analysis. Statistical analysis was performed using GraphPad Prism 8 (GraphPad Software Inc., CA, USA). Statistical significance of the differences between means of gene expressions was determined with the unpaired t-test. P values < 0.05 were considered statistically significant. In other experiments, one-way ANOVA statistical analysis was used to calculate the significance of the data, $\alpha = 0.05$.

Received: 19 September 2019; Accepted: 24 January 2020;
Published online: 17 February 2020

36

References

1. Dadfar, S. M. *et al*. Iron oxide nanoparticles: Diagnostic, therapeutic and theranostic applications. *Advanced Drug Delivery Reviews* **138**, 302–325 (2019).
2. Haracz, S., Mrōz, B., Rybka, J. D. & Giersig, M. Magnetic behaviour of non-interacting colloidal iron oxide nanoparticles in physiological solutions. *Cryst. Res. Technol.* **50**, 791–796 (2015).
3. Rybka, J. D. Radiosensitizing properties of magnetic hyperthermia mediated by superparamagnetic iron oxide nanoparticles (SPIONs) on human cutaneous melanoma cell lines. *Reports of Practical Oncology and Radiotherapy*, https://doi.org/10.1016/j.rpor.2019.01.002 (2019).
4. Kucharczyk, K. *et al*. Composite spheres made of bioengineered spider silk and iron oxide nanoparticles for theranostics applications. *Plos One*, https://doi.org/10.1371/journal.pone.0219790 (2019).
5. Kręcisz, M. *et al*. Interactions between magnetic nanoparticles and model lipid bilayers - Fourier transformed infrared spectroscopy (FTIR) studies of the molecular basis of nanotoxicity. *J. Appl. Phys.* **120**, 124701 (2016).
6. Tassa, C., Shaw, S. Y. & Weissleder, R. Dextran-coated iron oxide nanoparticles: A versatile platform for targeted molecular imaging, molecular diagnostics, and therapy. *Acc. Chem. Res.* **44**, 842–852 (2011).
7. Gaihre, B., Khil, M. S., Lee, D. R. & Kim, H. Y. Gelatin-coated magnetic iron oxide nanoparticles as carrier system: Drug loading and *in vitro* drug release study. *Int. J. Pharm.* **365**, 180–189 (2009).
8. Kayal, S. & Ramanujan, R. V. Doxorubicin loaded PVA coated iron oxide nanoparticles for targeted drug delivery. *Mater. Sci. Eng. C* **30**, 484–490 (2010).
9. Schleich, N. *et al*. Dual anticancer drug/superparamagnetic iron oxide-loaded PLGA-based nanoparticles for cancer therapy and magnetic resonance imaging. *Int. J. Pharm.* **447**, 94–101 (2013).
10. Ma, H. L., Qi, X. R., Maitani, Y. & Nagai, T. Preparation and characterization of superparamagnetic iron oxide nanoparticles stabilized by alginate. *Int. J. Pharm.* **333**, 177–186 (2007).
11. Unsoy, G., Yalcin, S., Khodadust, R., Gunduz, G. & Gunduz, U. Synthesis optimization and characterization of chitosan coated iron oxide nanoparticles produced for biomedical applications. *J. Nanoparticle Res.* **14**, 964 (2012).
12. Xie, J. *et al*. Human serum albumin coated iron oxide nanoparticles for efficient cell labeling. *Chem. Commun.* **46**, 433–435 (2010).
13. Huang, J. *et al*. Casein-coated iron oxide nanoparticles for high MRI contrast enhancement and efficient cell targeting. *ACS Appl. Mater. Interfaces* **5**, 4632–4639 (2013).
14. Lin, L. S. *et al*. Multifunctional Fe3O4@polydopamine core-shell nanocomposites for intracellular mRNA detection and imaging-guided photothermal therapy. *ACS Nano* **8**, 3876–3883 (2014).
15. Sun, W., Mignani, S., Shen, M. & Shi, X. Dendrimer-based magnetic iron oxide nanoparticles: their synthesis and biomedical applications. *Drug Discovery Today* **21**, 1873–1885 (2016).
16. García-Jimeno, S. & Estelrich, J. Ferrofluid based on polyethylene glycol-coated iron oxide nanoparticles: Characterization and properties. *Colloids Surfaces A Physicochem. Eng. Asp.* **420**, 74–81 (2013).
17. Huang, J. *et al*. Effects of nanoparticle size on cellular uptake and liver MRI with polyvinylpyrrolidone-coated iron oxide nanoparticles. *ACS Nano* **4**, 7151–7160 (2010).
18. Pareek, V. *et al*. Formation and Characterization of Protein Corona Around Nanoparticles: A Review. *J. Nanosci. Nanotechnol.* **18**, 6653–6670 (2018).
19. Stepien, G. *et al*. Effect of surface chemistry and associated protein corona on the long-term biodegradation of iron oxide nanoparticles *in Vivo*. *ACS Appl. Mater. Interfaces* **10**, 4548–4560 (2018).
20. Rybka, J. D. *et al*. Assembly and Characterization of HBc Derived Virus-like Particles with Magnetic Core. *Nanomater. (Basel, Switzerland)* **9** (2019).
21. IR Spectrum Table & Chart | Sigma-Aldrich. Available at, https://www.sigmaaldrich.com/technical-documents/articles/biology/ir-spectrum-table.html (Accessed: 25th November 2019).
22. Infrared Spectroscopy. Available at, https://www2.chemistry.msu.edu/faculty/reusch/VirtTxtJml/Spectrpy/InfraRed/infrared.htm (Accessed: 25th November 2019).
23. Ahangaran, F., Hassanzadeh, A. & Nouri, S. Surface modification of Fe3O4@SiO2 microsphere by silane coupling agent. *Int. Nano Lett.* **3** (2013).
24. Wierzbinski, K. R. *et al*. Potential use of superparamagnetic iron oxide nanoparticles for *in vitro* and *in vivo* bioimaging of human myoblasts. *Sci. Rep.* **8** (2018).
25. Milto, I. V., Suhodolo, I. V., Prokopieva, V. D. & Klimenteva, T. K. Molecular and cellular bases of iron metabolism in humans. *Biochemistry (Moscow)* **81**, 549–564 (2016).
26. Shen, Y. *et al*. Transferrin receptor 1 in cancer: a new sight for cancer therapy. *Am. J. Cancer Res.* **8**, 916–931 (2018).
27. Aisen, P. Transferrin receptor 1. *International Journal of Biochemistry and Cell Biology* **36**, 2137–2143 (2004).
28. Arosio, P. & Levi, S. Ferritin, iron homeostasis, and oxidative damage. *Free Radic. Biol. Med.* **33**, 457–463 (2002).
29. Lartigue, L. *et al*. Biodegradation of iron oxide nanocubes: High-resolution *in situ* monitoring. *ACS Nano* **7**, 3939–3952 (2013).
30. Pawelczyk, E., Arbab, A. S., Pandit, S., Hu, E. & Frank, J. A. Expression of transferrin receptor and ferritin following ferumoxides-protamine sulfate labeling of cells: Implications for cellular magnetic resonance imaging. *NMR Biomed.* **19**, 581–592 (2006).
31. Sharma, U., Pal, D. & Prasad, R. Alkaline phosphatase: An overview. *Indian Journal of Clinical Biochemistry* **29**, 269–278 (2014).
32. Seshacharyulu, P., Pandey, P., Datta, K. & Batra, S. K. Phosphatase: PP2A structural importance, regulation and its aberrant expression in cancer. *Cancer Letters* **335**, 9–18 (2013).
33. Tonks, N. K. Protein tyrosine phosphatases: From genes, to function, to disease. *Nature Reviews Molecular Cell Biology* **7**, 833–846 (2006).
34. Olsen, J. V. *et al*. Global, *In Vivo*, and Site-Specific Phosphorylation Dynamics in Signaling Networks. *Cell* **127**, 635–648 (2006).
35. Qu, C. K. Role of the SHP-2 tyrosine phosphatase in cytokine-induced signaling and cellular response. *Biochimica et Biophysica Acta - Molecular Cell Research* **1592**, 297–301 (2002).
36. Neel, B. G., Gu, H. & Pao, L. The 'Shp'ing news: SH2 domain-containing tyrosine phosphatases in cell signaling. *Trends in Biochemical Sciences* **28**, 284–293 (2003).
37. Mieloch, A. A. *et al*. The influence of ligand charge and length on the assembly of Brome mosaic virus derived virus-like particles with magnetic core. *AIP Adv*. **8** (2018).
38. Gu, J. L. *et al*. The internalization pathway, metabolic fate and biological effect of superparamagnetic iron oxide nanoparticles in the macrophage-like RAW264.7 cell. *Sci. China Life Sci.* **54**, 793–805 (2011).
39. Fu, P. P., Xia, Q., Hwang, H. M., Ray, P. C. & Yu, H. Mechanisms of nanotoxicity: Generation of reactive oxygen species. *Journal of Food and Drug Analysis* **22**, 64–75 (2014).
40. Wu, H., Yin, J. J., Wamer, W. G., Zeng, M. & Lo, Y. M. Reactive oxygen species-related activities of nano-iron metal and nano-iron oxides. *Journal of Food and Drug Analysis* **22**, 86–94 (2014).
41. Sakulkhu, U., Mahmoudi, M., Maurizi, L., Salaklang, J. & Hofmann, H. Protein corona composition of superparamagnetic iron oxide nanoparticles with various physico-Chemical properties and coatings. *Sci. Rep*. **4** (2014).
42. Mieloch, A. A. *et al*. The influence of ligand charge and length on the assembly of Brome mosaic virus derived virus-like particles with magnetic core. *AIP Adv.* **8**, 035005 (2018).

Acknowledgements
This work was supported by the National Centre for Research and Development LIDER/34/0122/L-9/17/NCBR/2018 and the National Science Centre UMO-2016/23/B/NZ7/01288 and UMO-2017/25/B/NZ5/01231 grants. The work was supported by grant no. POWR.03.02.00-00-I026/16 co-financed by the European Union through the European Social Fund under the Operational Program Knowledge Education Development.

Author contributions
Conceptualization of the research: A.A.M. and J.D.R.; Design of the experiments: A.A.M., N.R. and J.D.R.; Data acquisition: A.A.M. and M.Z.; Data analysis: A.A.M., M.Z., N.R. and J.D.R.; Lab work: A.A.M. and M.Z.; Manuscript preparation: A.A.M., M.Z., M.G., N.R. and J.D.R.; Supervision: N.R. and J.D.R.

Competing interests
The authors declare no competing interests.

Additional information
Supplementary information is available for this paper at https://doi.org/10.1038/s41598-020-59478-2.

Correspondence and requests for materials should be addressed to J.D.R.

Reprints and permissions information is available at www.nature.com/reprints.

Publisher's note Springer Nature remains neutral with regard to jurisdictional claims in published maps and institutional affiliations.

Open Access This article is licensed under a Creative Commons Attribution 4.0 International License, which permits use, sharing, adaptation, distribution and reproduction in any medium or format, as long as you give appropriate credit to the original author(s) and the source, provide a link to the Creative Commons license, and indicate if changes were made. The images or other third party material in this article are included in the article's Creative Commons license, unless indicated otherwise in a credit line to the material. If material is not included in the article's Creative Commons license and your intended use is not permitted by statutory regulation or exceeds the permitted use, you will need to obtain permission directly from the copyright holder. To view a copy of this license, visit http://creativecommons.org/licenses/by/4.0/.

© The Author(s) 2020

View publication stats

nanomaterials

MDPI

Article

Assembly and Characterization of HBc Derived Virus-like Particles with Magnetic Core

Jakub Dalibor Rybka [1,†,*], Adam Aron Mieloch [1,2,†], Alicja Plis [1], Marcin Pyrski [3], Tomasz Pniewski [3] and Michael Giersig [1,4]

1 Center for Advanced Technology, Adam Mickiewicz University in Poznań, Umultowska 89C, 61-614 Poznań, Poland; amieloch@amu.edu.pl (A.A.M.); alkaplis@o2.pl (A.P.); giersig@amu.edu.pl (M.G.)
2 Faculty of Chemistry, Adam Mickiewicz University in Poznań, Umultowska 89B, 61-614 Poznań, Poland
3 Institute of Plant Genetics, Polish Academy of Sciences, Strzeszyńska 34, 60-479 Poznań, Poland; mpyr@igr.poznan.pl (M.P.); tpni@igr.poznan.pl (T.P.)
4 Institute of Experimental Physics, Freie Universität Berlin, Arnimallee 14, 14195 Berlin, Germany
* Correspondence: jrybka@amu.edu.pl; Tel.: +48-61-829-1875
† These authors contributed equally to this work.

Received: 20 December 2018; Accepted: 24 January 2019; Published: 26 January 2019

Abstract: Core-virus like particles (VLPs) assembly is a kinetically complex cascade of interactions between viral proteins, nanoparticle's surface and an ionic environment. Despite many in silico simulations regarding this process, there is still a lack of experimental data. The main goal of this study was to investigate the capsid protein of hepatitis B virus (HBc) assembly into virus-like particles with superparamagnetic iron oxide nanoparticles (SPIONs) as a magnetic core in relation to their characteristics. The native form of HBc was obtained via agroinfection of *Nicotiana benthamiana* with pEAQ-HBc plasmid. SPIONs of diameter of 15 nm were synthesized and functionalized with two ligands, providing variety in ζ-potential and hydrodynamic diameter. The antigenic potential of the assembled core-VLPs was assessed with enzyme-linked immunosorbent assay (ELISA). Morphology of SPIONs and core-VLPs was evaluated via transmission electron microscopy (TEM). The most successful core-VLPs assembly was obtained for SPIONs functionalized with dihexadecyl phosphate (DHP) at SPIONs/HBc ratio of 0.2/0.05 mg/mL. ELISA results indicate significant decrease of antigenicity concomitant with core-VLPs assembly. In summary, this study provides an experimental assessment of the crucial parameters guiding SPION-HBc VLPs assembly and evaluates the antigenicity of the obtained structures.

Keywords: virus-like particles; VLPs; hepatitis B virus capsid protein; HBc; viral self-assembly; magnetic core; HBcAg

1. Introduction

Virus-like particles (VLPs) are non-infectious and non-replicating supramolecular assemblies composed of single or multiple viral proteins, which closely resemble native virions [1]. VLPs display a unique set of immunological characteristics that render them highly potent for vaccine development such as: nanometer range size, multivalent and highly repetitive surface geometry, the ability to elicit both innate and adaptive immune response [2]. Due to favorable surface morphology and a wide range of possible modifications, VLPs have been successfully used as a platform for multivalent vaccine creation [3–5]. Several VLP-based vaccines are currently commercially available (e.g., Cervarix®, Gardasil®, Sci-B-Vac™, Mosquirix™) with more undergoing clinical trials [6]. VLPs' applicability is not limited to their immunogenic properties. Some of the use cases include: highly selective and sensitive nanobiosensor for troponin I detection, light-harvesting VLPs for use in photovoltaic or

photocatalytic devices, nanofiber-like VLPs for tissue regenerating materials, nanocontainers and nanoreactors [7–11].

Hepatitis B virus (HBV) is an enveloped, icosahedral, cDNA virus that belongs to the Hepadnaviridae family. The virion has a diameter of 42 nm and is composed of a lipid envelope with hepatitis B virus surface antigen (HBsAg) and inner nucleocapsid consisting of hepatitis B virus capsid protein—HBc (named also HB core antigen, HBcAg) [12]. HBc consists of 183–185 amino acids of which 149 N-terminal amino acids form an assembly domain and 34 amino acids form C-terminal arginine-rich domain (CTAD) required for the packaging of nucleic acid [13]. HBc is a homodimeric protein that has the ability to self-assemble into icosahedral and fenestrated T = 4 (120 dimers) and T = 3 (90 dimers) capsids with respective outer diameter of 34 and 30 nm [14]. T = 4 capsid is a dominant product of a wild type HBc in vitro self-assembly (~95%) [15]. HBc capsid is highly immunogenic and has been shown to induce both B- and T-cell response [16].

Superparamagnetic iron oxide nanoparticles (SPIONs) exhibit properties, such as high magnetic susceptibility, high saturation magnetization and low toxicity [17–19]. Due to the aforementioned properties, high-yield synthesis methods and a wide array of available surface modifications, SPIONs can be utilized in: magnetic bioseparation, magnetic hyperthermia, targeted drug delivery, in diagnostics as magnetic resonance imaging (MRI) contrast agents, etc. [20–23].

Introduction of SPIONs as the core of VLPs has been performed successfully with several viral proteins of different origin [24–26]. Magnetic core adds a multitude of advantageous properties. It allows for post-assembly magnetic bioseparation, which may be crucial for large scale production [27]. It also improves cellular uptake and magnetic relaxivities resulting in higher resolution MRI images, which combined with in vivo tracking may provide essential data regarding VLPs biodistribution [28]. Functionalized core can act as a substitute for native nucleic acid, and therefore, govern the process of protein recruitment and organization during self-assembly. Rational core design can be used to facilitate the assembly and enhance such parameters as, e.g., physicochemical stability, mechanical elasticity, capacity to withstand desiccation and long-term storage. On the other hand, HBc VLPs have been shown to be potent epitope carriers [3,29].

In the study by Shen et al., HBc was genetically engineered into a truncated version, deprived of 34 C-terminal amino acids responsible for nucleic acid packaging. The removed part was replaced by six consecutive histidine residues (His-tag). Fe_3O_4 nanoparticles functionalized with nickel-nitrilotriacetic acid (nickel-NTA) chelate were used as the core. The VLPs assembly was driven by the affinity of histidine tags to the nickel-NTA chelate [28]. This study prompted us to investigate whether native HBc VLPs assembly can be successful, without resorting to genetic engineering of HBc protein.

The main objective of this study was to investigate whether provided SPION surface modification is sufficient for SPION-HBc assembly. Even though HBc subunits exhibit an ability to assemble in the absence of genetic material, electrostatic interactions between positively charged CTAD of the capsid and negatively charged nucleic acid have a major influence on the assembly process [30]. Therefore, to mimic native electrostatic interactions, negatively charged ligands were chosen for SPIONs functionalization: dihexadecyl phosphate (DHP) and PL-PEG-COOH. Both compounds were successfully used in our previous study regarding the influence of ligand charge and length on the assembly of Brome mosaic virus derived virus-like particles with magnetic core [31].

2. Materials and Methods

2.1. Reagents

Oleic acid (technical grade 90%), Iron (III) acetylacetonate (97%), Sodium chloride (99%), Dihexadecyl phosphate (90%), 1-Octadecene (90%), 2-Butanol (95.5%), Trizma®hydrochloride (99%), Calcium chloride (97%), Magnesium sulfate (99.5%), Glycine (99%), Glycerol (99%), Urea (98%), 2-(N-Morpholino)ethanesulfonic acid (99%), Sucrose (99.5%), Sigma-Aldrich (Poznan, Poland). Toluene (99.5%), n-Hexane (99%), Chloroform (98.5%) and Hydrochloric acid (30–35%), Avantor (Gliwice,

Poland). 1,2-Distearoyl-sn-glycero-3-phosphoethanolamine-N-[carboxy-(polyethyleneglycol)-2000] (ammonium salt) (PL-PEG-COOH, 2000 Da PEG (99%), Avanti, Alabaster, AL, USA). Snakeskin®Dialysis Tubing, 10K MWCO, 22 mm, Thermo Fisher Scientific (Waltham, MA, USA). All chemicals were used as received. Water was purified with Hydrolab HLP5 instrument (0.09 µS/cm, Straszyn, Poland).

2.2. Superparamagnetic Iron Oxide Nanoparticles (SPIONs) Synthesis

Spherical iron oxide nanoparticles were synthesized via thermal decomposition of iron (III) acetylacetonate $Fe(acac)_3$ [32]. Briefly, 6 mmol of $Fe(acac)_3$ and 18 mmol of oleic acid were dissolved in 40 mL of 1-octadecene. The reaction was performed with continuous stirring and nitrogen flow. Temperature of the solution was increased to 220 °C and maintained for 1 h. Subsequently, the temperature was increased further to 320 °C and maintained for 1 h. After synthesis, the solution was left to cool down to ambient temperature and 200 mL of washing solution (3:1 v/v of 2-butanol and toluene) was added. The obtained mixture was placed on a neodymium magnet and left overnight to allow nanoparticles to precipitate. Supernatant was discarded and replaced with fresh washing solution. Sonicating bath was used to resuspend nanoparticles. The washing step was performed thrice. In the final step, nanoparticles were suspended in 20 mL of chloroform. Concentration of the nanoparticles was estimated by dried sample weighing.

2.3. SPIONs Functionalization

PL-PEG-COOH functionalization was performed as per a method published elsewhere [24], with minor modifications. Briefly, 3.0 mg of PL-PEG-COOH were added to 5 mL of 1.0 mg/mL SPIONs chloroform solution. The sample was briefly sonicated in a sonic bath and left open for chloroform evaporation. The obtained waxy solid was heated for 1 min in an 80 °C water bath. The following step was adding 5 mL of miliQ water and vortexing the sample to enhance micelles formation. Subsequently, the sample was washed thrice with chloroform to remove unbound PL-PEG-COOH. Finally, water phase containing functionalized SPIONs was collected and filtered through 0.22 µm pores. Concentration of the SPION-PEG nanoparticles was measured via thermogravimetric analysis described below.

DHP functionalization was performed as per a method published elsewhere [31], with minor modifications. Briefly, 10.0 mg of dihexadecyl phosphate were added to 20 mL of hexane and dissolved with heat-assisted magnetic stirring (75 °C, ca. 10 min). After DHP dissolution, a chloroform solution containing 10.0 mg of synthesized iron oxide nanoparticles coated with oleic acid was added. The mixture was shortly sonicated and 80 mL of water were added. Subsequently, the obtained two phase solution was briefly vortexed and sonicated until the water phase became turbid. In the next step, the solution was placed in a sonicating bath for 3–4 h with no temperature control exercised. After functionalization, the solution was left overnight to allow for phase separation. The Bobtom phase was collected and placed near neodymium magnet for 24 h to separate functionalized nanoparticles from the solution. The obtained precipitate was collected, suspended in 2 mL of miliQ water and filtered through 0.22 µm pores. Concentration of the SPION-DHP nanoparticles was measured via thermogravimetric analysis described below.

2.4. Concentration Measurement via Thermogravimetric Analysis

Thermogravimetric analysis was performed to measure concentrations of the functionalized SPIONs. The analysis was performed on TGA 4000 System (Perkin Elmer apparatus, Waltham, MA, USA). Briefly, a 20 µL sample was taken for measurement. Each sample was measured in triplicate. The sample was heated from 20 to 150 °C at 10 °C/min in nitrogen atmosphere. The lowest mass was taken as fully dried sample and used for further calculations. The obtained mass was normalized for 20 mg of the initial sample mass. The mean of three measurements was calculated. Density was derived from

weighing 5 × 15 µL of the sample and dividing the mean mass by volume. Final concentrations were: SPION-DHP = 3.52 mg/mL and SPION-PEG = 3.81 mg/mL.

2.5. HBc Production and Preparation

HBc was produced in plants via a transient expression system based on agroinfiltration. HBc expression vector was constructed on the basis of pEAQ-HT plasmid, developed by Peyret and Lomonossoff [33]. The coding sequence of HBcAg of 552 bp in length derived from HBV subtype *adw4* (GenBank: Z35717), was cloned into the vector *Age* I and *Xho* I restriction sites using sites *Age* I and compatible ends of *Sal* I, respectively, introduced by PCR using the following primers:

Forward: AACCGGTATGGACATTGACCCTTATAAAGAATTTG

Reverse: TGTCGACTGCAGTTAACATTGAGATTCCCGAGATTGAG

Complete vector pEAQ-HBc was introduced into *Agrobacterium tumefaciens* EHA105 and LBA4404 strains via electroporation.

Agroinfection was performed with *Agrobacterium* strains grown overnight on selective liquid LB medium supplemented with kanamycin (50 mg/l) and used to infiltrate leaves of 5–7 week-old *Nicotiana benthamiana* plants, cultivated in growth chamber under 5–6 klx light intensity, 16/8 h photoperiod and at a 22/16 °C temperature regime. *Agrobacterium* cells were centrifuged at 2000 g for 3 min at 4 °C and resuspended in MES buffer (10 mM 2-(N-morpholino)ethanesulphonic acid, 10 mM $MgSO_4$, pH 5.7) to optical density at a 600 nm wavelength (OD_{600}) 0.6 or 0.1 for infiltration by syringe or exsiccator, respectively. *Agrobacterium* suspension, 0.5 mL per leaf, was injected with a syringe into the bottom side of the leaves. Alternatively, whole plants were inverted and immersed in 2 L of *Agrobacterium* suspension in exsiccator (Lab Companion VDP-25G, Seoul, Korea). Pump (AGA Labor PL2, Poznań, Poland) was then applied to reach underpressure (−0.08 MPa) for approximately 1 min. The vacuum was released and applied again to ensure infiltration of the whole leaves. After 10 days following the agroinfiltration concentration of HBc in plant tissue reached approximately 1 mg/g of fresh weight (data not shown). HBc was then extracted and partially purified using sucrose density gradient as described previously [33]. The concentration of HBc directly after purification was fixed to 0.1 mg/mL. Prior to SPION encapsulation, HBc was diluted twice in a disassembly buffer.

2.6. SPION-HBc Preparation

VLPs were prepared in line with a slightly modified procedure described elsewhere [28].

HBc dissociation: 300 µL of 0.1 mg/mL HBc were diluted with 300 µL of denaturant solution (5 M urea, 300 mM NaCl, 100 mM tris-HCl) and incubated at 25 °C for 3h.

SPION-HBc assembly: The solution of dissociated HBc was divided into 100 µL aliquots (HBc conc. 0.05 mg/mL). To each aliquot, functionalized SPIONs were added to a final concentration of 0.5, 1.0 and 2.0 mg/mL. Obtained solutions were dialyzed twice against 400 mL of assembly buffer (150 mM NaCl, 10 mM $CaCl_2$, 1% *w*/*v* glycine, 10% *v*/*v* glycerol, 50 mM tris-HCl, pH = 8) for 24 h at 4 °C.

2.7. VLPs Antigenicity

Antigenicity of HBc VLPs was assessed via enzyme-linked immunosorbent assay (ELISA). HBc assembled with functionalized SPION-PEG and SPION-DHP at different concentrations (mg/mL) in comparison to the standard protein (recombined in *E. coli*, Cat No. R8A120, Meridian Life Science Inc., Memphis, TN, USA). Antigenicity defined as absorbance at 405 nm of two-fold dilution series of VLPs (from 1:160 to 1:81,920) and standard protein (from 0.5 to 0.004 µg/mL).

2.8. Statistical Analysis

Results of SPION-HBc formation were analyzed using a two-way ANOVA followed by a Duncan test; differences were considered significant at $p \leq 0.05$. Statistical analysis was performed using the Statistica 8.0 statistical software package (StatSoft Inc., Tulsa, OK, USA).

2.9. Characterization Methods

Transmission electron microscopy (TEM) images were acquired with Hitachi TEM HT7700 microscope (Tokyo, Japan). Grids were made of copper coated with a carbon film, mesh 300. Samples were prepared by placing 15 µL drop on the grid and draining the excess solution with blotting paper and left for 15 min. to dry. Subsequently, samples were negatively stained with 10 µL of 2% uranyl acetate. Particle size analysis was performed with free ImageJ software version 1.51w (NIH, Bethesda, MD, USA).

Dynamic light scattering (DLS) and ζ-potential measurements were performed on Malvern Zetasizer Nano ZS90 (Worcestershire, UK) in a Folded Capillary Zeta Cell DTS1070. Prior to measurement, samples were briefly sonicated, diluted to optimal concentration and filtered with a 0.2 µm syringe filter (Merck Millipore, Burlington, MA, USA). Measurements were repeated in triplicate.

ELISA was performed on the assembled HBc VLPs, with or without SPION core. The assay was performed in line with a procedure described previously [34]. MaxiSorp (NUNC) 96-well microplate was coated overnight at 4 °C with of HBc-specific mAb (0.5 mg/mL) (Cat. No. C31190 M, Meridian Life Science Inc., Memphis, TN, USA) in carbonate buffer pH 9.6. Each step following the coating was preceded by three washes with PBST buffer (phosphate buffered saline with additional 0.05% *v*/*v* Tween20, Sigma, Saint Louis, MO, USA). The coated wells were blocked for 1 h with 5% (*w*/*v*) fat-free milk/PBS, followed by incubation with 100 µL of antibody solution for 1 h at 25 °C. The samples were added to the PBS-filled wells and two-fold serially diluted. HBc produced in *E. coli* (Cat. No. R8A120, Meridian Life Science) was used as the reference. Rabbit polyclonal PBST antibody specific to HBc (Cat. No. LS-C67451/18649, Life Span Biosciences, Seattle, VA, USA) 0.125 mg/mL and goat anti-rabbit whole-molecule polyclonal antibody AP-conjugated (Sigma) 1:10,000 dilutions were premixed and added as the primary and secondary antibody. Finally, the substrate for alkaline phosphatase (pNPP, Sigma) was added and the reaction was developed at 25 °C for at least 30 min. The absorbance was measured at 405 nm using a microplate reader (Model 680, Bio-Rad, Hercules, CA, USA).

3. Results

3.1. SPIONs Synthesis and Functionalization

Monodispersed superparamagnetic iron oxide nanoparticles (SPIONs) of 15 nm diameter were synthesized via thermal decomposition of iron (III) acetylacetonate $Fe(acac)_3$ (Figure S1). The approximate diameter of the HBc VLP internal cavity is 25 nm for the T = 4 particles and 21 nm for the T = 3 [14]. Therefore, both structures provide sufficient marginal space to accommodate the ligands. In order to obtain negative surface charge, SPIONs were functionalized with short and long chain ligands: dihexadecyl phosphate (DHP) and 1,2-distearoyl-sn-glycero-3-phosphoethanolamine-N-[carboxy-(polyethylene glycol)-2000] (PL-PEG-COOH) (Figure 1a,b). Functionalized SPIONs will be denoted as SPION-DHP and SPION-PEG, respectively.

DHP functionalization was performed according to our previously described method [31]. PL-PEG-COOH functionalization was achieved by a slightly modified protocol by Huan et al. [24]. Both SPION-DHP and SPION-PEG were analyzed via ζ-potential and dynamic light scattering (DLS) measurements (Table 1). In both cases, functionalization is driven by hydrophobic interactions between oleic acid residues present on the surface of as-obtained SPIONs and alkyl chains of the ligands. More detailed characterization of both functionalizations can be found in our previous work [31].

Despite rather small differences in surface charge, hydrodynamic radius differs substantially. Counterintuitively, long-chain PEG ligand provided smaller hydrodynamic radius than DHP, which may be partially caused by differences in ζ-potential. Another plausible explanation is the interplay of surface charge and multilayered micelle structure formation.

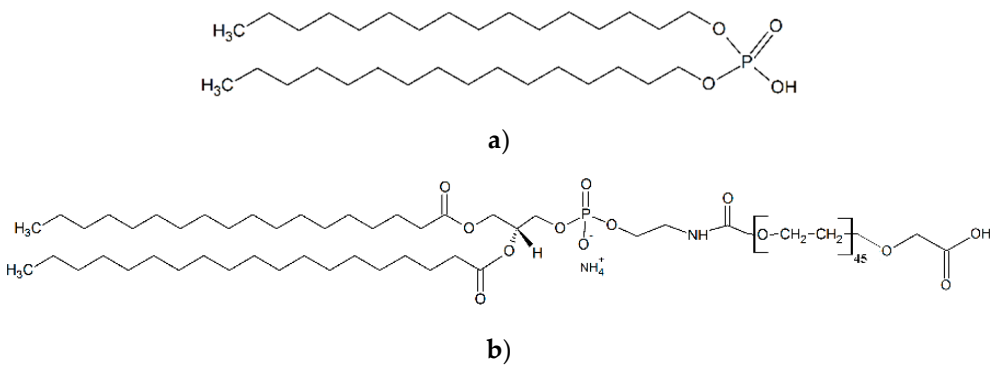

Figure 1. Molecular structure of ligands used for superparamagnetic iron oxide nanoparticles (SPIONs) functionalization. (**a**) dihexadecyl phosphate (DHP); (**b**) 1,2-distearoyl-sn-glycero-3-phosphoethanolamine-N-[carboxy-(polyethylene glycol)-2000] (PL-PEG-COOH).

Table 1. ζ-potential and hydrodynamic radius of the functionalized superparamagnetic iron oxide nanoparticles (SPIONs) obtained by dynamic light scattering (DLS) (Figures S2 and S3).

	SPION-DHP	SPION-PEG
ζ-potential	−44.0 ± 3.4 mV	−37.3 ± 2.9 mV
Hydrodynamic diameter	53.75 ± 1.93 nm	29.69 ± 1.57 nm

3.2. VLPs-SPION Assembly

The assembly rates and core encapsidation efficiency are strictly dependent on surface charge density, capsid protein concentration and core/capsid protein stoichiometric ratio [35]. Therefore, HBc concentration was fixed at 0.05 mg/mL while SPIONs concentrations were varied between: 0.05, 0.1 and 0.2 mg/mL. It is important to note that due to differences in ligands' molecular weight and probable differences in functionalization densities, equal w/v concentrations of SPION-PEG and SPION-DHP do not represent the same amount of particles in the solution. The most successful core-VLP assembly was obtained at following concentrations: 0.2 mg/mL SPION-DHP and 0.05 mg/mL SPION-PEG (Figure 2a,b).

TEM images were used to measure the diameter of the assembled VLPs. Mean diameter of SPION-DHP-HBc was 28.4 ± 1.2 nm while SPION-PEG-HBc mean diameter was 29.9 ± 1.5 nm (Table 2). The obtained measurements indicate that in both cases capsids assembled into T = 3 symmetry (native size of T = 3 capsid is 30 nm). Nonetheless, to assess the VLPs symmetry with certainty, crystallographic studies would be required. The obtained results are concordant with thermodynamic studies of nanospheres encapsulated in virus capsids reveling, in that core surface charge and its radius determine the size of the capsid formed around the nanoparticle [36]. In this case, despite T = 4 symmetry being a predominant form of in vitro HBc self-assembly (~95%), introduction of SPION-DHP and SPION-PEG facilitated assembly into a smaller, presumably T = 3 form. This may suggest that negative surface charge density was high enough to drive the assembly into less energetically-favorable capsid morphology. Studying TEM images, SPION-DHP assembly displayed higher efficiency than SPION-PEG and resulted in minority of empty capsids and unassembled cores. In comparison, SPION-PEG assembly produced a multitude of empty capsids along with unassembled cores.

Table 2. VLPs diameter measurements obtained from transmission electron microscopy (TEM) images. Measured with ImageJ software.

	SPION-DHP-HBc	SPION-PEG-HBc
Diameter	28.4 ± 1.2 nm	29.9 ± 1.5 nm
Number of measured VLPs	41	19

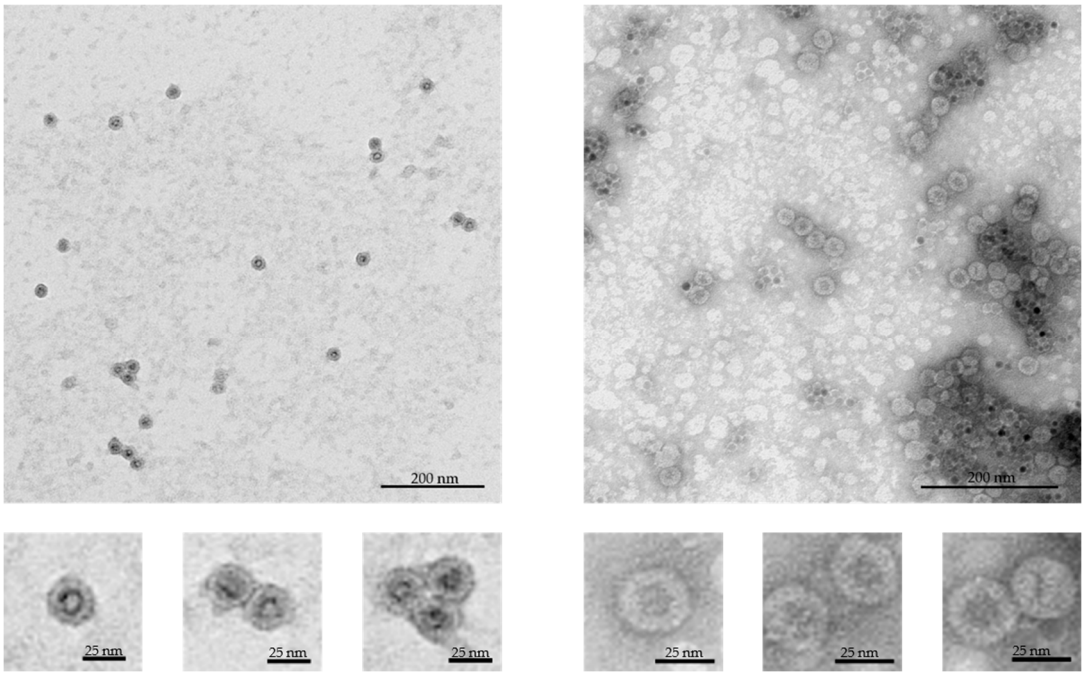

Figure 2. Transmission electron microscopy (TEM) images of the assembled VLPs with magnetic cores, negatively stained with 2% uranyl acetate. (**a**) SPION-DHP-HBc VLPs obtained at 0.2 mg/mL of SPION-DHP and 0.05 mg/mL of HBc; (**b**) SPION-PEG-HBc VLPs obtained at 0.05 mg/mL of SPION-PEG and 0.05 mg/mL of HBcAg.

3.3. VLPs ELISA

Antigenicity of the obtained VLPs was assessed via ELISA (Figures 3 and S4). Despite unvaried HBc protein concentrations, for all VLPs variants decreased signals of HBc detection in comparison to control (initial HBc used) were observed, as well as some significant differences in signals among VLPs variants were found. All concentrations of SPION-PEG displayed a decrease in signal intensity; however, the differences between 0.05 and 0.1 mg/mL concentrations were not statistically significant. Additionally, in comparison to analogous variants of SPION-DHP. For SPION-PEG, the highest observed amount of core-VLPs was found at 0.05 mg/mL (Figure 2B), which also resulted in decreased signal intensity, although insignificantly different from other SPION-PEG concentrations. Finally, among all variants of SPION-HBc VLPs, the significantly lowest signal, 61.6% of HBc was recorded for 0.2 mg/mL SPION-DHP, the same concentration at which the highest number of core-VLPs was observed. The obtained results indicate that core introduction into HBc derived VLPs may decrease antigenicity. This phenomenon could be explained by the proclivity of HBcAg to assemble into smaller T = 3 capsids in the presence of the SPIONs, which in turn results in higher antigen density on the VLPs surface and competitive binding of antibodies. A study by Wu et al. has shown that the amount of antibodies bound to the capsid depends on its morphology and is significantly decreased for T = 3 capsids [37]. Moreover, steric hindrance has been proven to be a crucial factor for antibody binding to surface antigens [38,39]. These results provide a great starting point for further investigations of the relationship between core properties, capsid morphology, antigenicity and biological activity of the HBc derived VLPs.

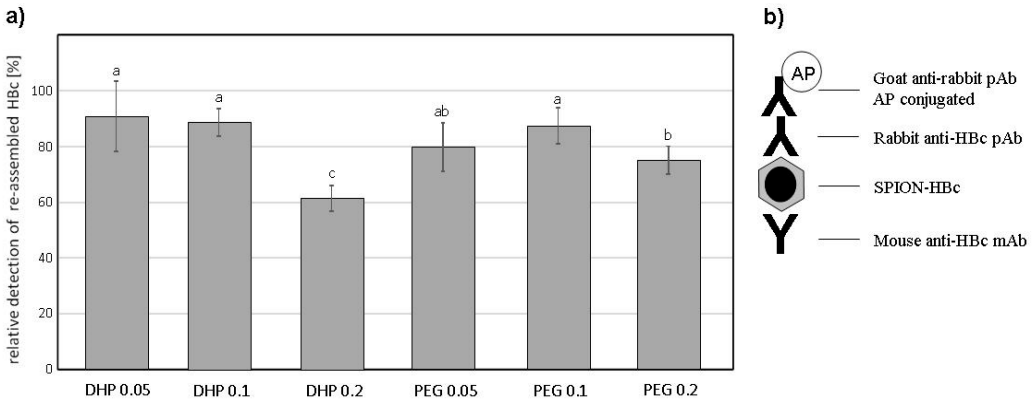

Figure 3. (**a**) HBc re-assembly on SPIONs functionalized with DHP or PEG in different concentrations (mg/mL) in comparison to the initial preparation of plant-derived antigen (100%). Statistically significant differences marked by a letter indexes; (**b**) Scheme of enzyme-linked immunosorbent assay (ELISA) test used for assay of VLP-assembled HBc and SPION-HBc VLPs. AP—alkaline phosphatase.

4. Discussion

Core-VLPs assembly, here SPION-HBc, is a kinetically complex cascade of interactions between viral proteins, nanoparticle surface and an ionic environment. In silico modeling predicts that core introduction provides a plethora of advantages such as increased assembly rates and efficiency over wider set of conditions, stimulation of the assembly below critical subunit concentration (CSC), possibility of templating VLPs morphology. Nonetheless, computational modeling results are not always confirmed in experimental studies. For example, the predicted increase of assembly efficiency driven by the increase of surface charge density has been overestimated in comparison to experimental data [35]. Moreover, simulations predominantly assume cores geometry perfectly commensurate with capsid interior. In our case, functionalized 15 nm SPIONs were not perfectly fitted into the capsid, which could elicit the existence of kinetic traps, not predicted by the computational studies [40]. The most successful core assembly was achieved at a 0.2/0.05 mg/mL core/protein ratio with SPION-DHP. Slightly lower ζ-potential concomitant with larger hydrodynamic diameter in comparison to SPION-PEG might indicate that surface charge density was higher in case of SPION-DHP. SPION-PEG assembly at 0.05/0.05 mg/mL core/protein ratio resulted in partially successful core assembly along with multitude of empty capsids and unassembled cores. This result indicates that one or several assembly parameters were suboptimal; however, due to the complexity of the process, we are unable to pinpoint the exact cause of lower efficiency. It is possible that interactions between less negatively charged SPION-PEG and positively charged domains of the HBc were insufficient to win competition over subunit-subunit attraction, resulting in the empty capsids. Additionally, it is important to note that the ligands used differed in length which could also affect assembly kinetics. In both cases, core introduction resulted in slightly smaller VLPs diameters even for T = 3 capsid morphology, which could be attributed to more compact HBc dimer-dimer spacing resulted from strong electrostatic core-HBc dimer interactions. This thesis stands in agreement with our experimental data showing smaller core-VLPs diameters for lower values of the core's ζ-potential (Table 2). VLPs morphology driven antigenicity is a crucial aspect determining its potential application, especially in the area of vaccinology. In that respect, our study demonstrated successful assembly together with substantially retained HBc antigenicity, although decreased in comparison to native HBc protein preparation containing mainly T = 4 capsids (Figure 3). This may indicate competitive binding of antibodies and/or steric clashes due to increased antigen surface density, stemming from the decreased VLPs diameter. Crucially, for many medical applications such as cell- or tissue-specific targeting, decreased immunogenicity of core antigen may be desirable. Nonetheless, this theory requires more in depth experimental investigation to be confirmed. Surface charge density is one of the most important parameters guiding core assembly. However, it is not easily measureable by standard lab equipment,

which impedes rational design of physicochemical properties of the core. Therefore, we propose the use of ζ-potential and hydrodynamic diameter, as two parameters encompassing surface charge density. This approach would simplify and unify core's surface electrostatic characterization, providing more accessible tool for core-VLPs design.

5. Conclusions

This study provides an experimental assessment of the crucial parameters guiding SPION-HBc VLPs assembly and evaluates antigenicity of the obtained structures. The presented results highlight potential directions for further studies regarding the mechanism guiding HBc VLPs assembly with metallic cores as well as their antigenic properties.

Supplementary Materials: The following are available online at http://www.mdpi.com/2079-4991/9/2/155/s1, Figure S1: TEM images of as synthesized SPIONs, Figure S2: DLS results for SPION-PEG and SPION-DHP, Figure S3: ζ-potential for SPION-DHP and SPION-PEG, Figure S4: ELISA of HBcAg SPION assembly.

Author Contributions: Conceptualization, J.D.R., A.A.M. and T.P.; Data curation, J.D.R., A.A.M., A.P. and M.P.; Formal analysis, J.D.R., A.A.M. and M.P.; Funding acquisition, J.D.R. and M.G.; Investigation, J.D.R., A.A.M., A.P. and M.P.; Methodology, J.D.R., A.A.M., M.P. and T.P.; Project administration, J.D.R.; Supervision, J.D.R., T.P. and M.G.; Validation, J.D.R. and A.A.M.; Visualization, A.A.M.; Writing—original draft, J.D.R. and A.A.M.; Writing—review & editing, J.D.R., A.A.M., M.P. and T.P.

Funding: This research was funded by the National Science Center, grant number UMO-2016/23/B/NZ7/01288 and by The National Centre for Research and Development, grant number LIDER/34/0122/L-9/NCBR/2018. HBc production and ELISA was funded by statutory funds of IPG PAS.

Acknowledgments: We are grateful to: Monika Kręcisz, CAT, UAM, for her contribution; Aleksandra Gryciuk, IPG PAS, for construction of vector for plant transient expression. In addition, we are grateful to Professor George Lomonossoff, John Innes Centre, Norwich, UK, for kindly providing the pEAQ-HT vector for transient expression of HBcAg in plants and to Plant Bioscience Ltd for allowing the material to be used.

Conflicts of Interest: The authors declare no conflict of interest.

References

1. López-Sagaseta, J.; Malito, E.; Rappuoli, R.; Bottomley, M.J. Self-assembling protein nanoparticles in the design of vaccines. *Comput. Struct. Biotechnol. J.* **2016**, *14*, 58–68. [CrossRef] [PubMed]
2. Bachmann, M.F.; Jennings, G.T. Vaccine delivery: a matter of size, geometry, kinetics and molecular patterns. *Nat. Rev. Immunol.* **2010**, *10*, 787–796. [CrossRef] [PubMed]
3. Sominskaya, I.; Skrastina, D.; Dislers, A.; Vasiljev, D.; Mihailova, M.; Ose, V.; Dreilina, D.; Pumpens, P. Construction and immunological evaluation of multivalent hepatitis B virus (HBV) core virus-like particles carrying HBV and HCV epitopes. *Clin. Vaccine Immunol.* **2010**, *17*, 1027–1033. [CrossRef] [PubMed]
4. Galarza, J.M.; Latham, T.; Cupo, A. Virus-Like Particle (VLP) Vaccine Conferred Complete Protection against a Lethal Influenza Virus Challenge. *Viral Immunol.* **2005**, *18*, 244–251. [CrossRef] [PubMed]
5. Jackwood, D.J. Multivalent Virus-Like–Particle Vaccine Protects Against Classic and Variant Infectious Bursal Disease Viruses. *Avian Dis.* **2013**, *57*, 41–50. [CrossRef] [PubMed]
6. Mohsen, M.O.; Zha, L.; Cabral-Miranda, G.; Bachmann, M.F. Major findings and recent advances in virus–like particle (VLP)-based vaccines. *Semin. Immunol.* **2017**, *34*, 123–132. [CrossRef]
7. Park, J.-S.; Cho, M.K.; Lee, E.J.; Ahn, K.-Y.; Lee, K.E.; Jung, J.H.; Cho, Y.; Han, S.-S.; Kim, Y.K.; Lee, J. A highly sensitive and selective diagnostic assay based on virus nanoparticles. *Nat. Nanotechnol.* **2009**, *4*, 259–264. [CrossRef]
8. Stephanopoulos, N.; Carrico, Z.M.; Francis, M.B. Nanoscale Integration of Sensitizing Chromophores and Porphyrins with Bacteriophage MS_2. *Angew. Chem. Int. Ed.* **2009**, *48*, 9498–9502. [CrossRef]
9. Merzlyak, A.; Indrakanti, S.; Lee, S.-W. Genetically Engineered Nanofiber-Like Viruses For Tissue Regenerating Materials. *Nano Lett.* **2009**, *9*, 846–852. [CrossRef]
10. De la Escosura, A.; Nolte, R.J.M.; Cornelissen, J.J.L.M. Viruses and protein cages as nanocontainers and nanoreactors. *J. Mater. Chem.* **2009**, *19*, 2274. [CrossRef]

11. Uchida, M.; Klem, M.T.; Allen, M.; Suci, P.; Flenniken, M.; Gillitzer, E.; Varpness, Z.; Liepold, L.O.; Young, M.; Douglas, T. Biological Containers: Protein Cages as Multifunctional Nanoplatforms. *Adv. Mater.* **2007**, *19*, 1025–1042. [CrossRef]
12. Liang, T.J. Hepatitis B: The virus and disease. *Hepatology* **2009**, *49*, S13–S21. [CrossRef]
13. Nassal, M. The arginine-rich domain of the hepatitis B virus core protein is required for pregenome encapsidation and productive viral positive-strand DNA synthesis but not for virus assembly. *J. Virol.* **1992**, *66*, 4107–4116. [PubMed]
14. Crowther, R.A.; Kiselev, N.A.; Böttcher, B.; Berriman, J.A.; Borisova, G.P.; Ose, V.; Pumpens, P. Three-dimensional structure of hepatitis B virus core particles determined by electron cryomicroscopy. *Cell* **1994**, *77*, 943–950. [CrossRef]
15. Zlotnick, A.; Palmer, I.; Kaufman, J.D.; Stahl, S.J.; Steven, A.C.; Wingfield, P.T. Separation and crystallization of T = 3 and T = 4 icosahedral complexes of the hepatitis B virus core protein. *Acta Crystallogr. Sect. D Biol. Crystallogr.* **1999**, *55*, 717–720. [CrossRef]
16. Milich, D.R.; McLachlan, A.; Moriarty, A.; Thornton, G.B. Immune response to hepatitis B virus core antigen (HBcAg): localization of T cell recognition sites within HBcAg/HBeAg. *J. Immunol.* **1987**, *139*, 1223–1231. [PubMed]
17. Haracz, S.; Mróz, B.; Rybka, J.D.; Giersig, M.; Mrõz, B.; Rybka, J.D.; Giersig, M. Magnetic behaviour of non-interacting colloidal iron oxide nanoparticles in physiological solutions. *Cryst. Res. Technol.* **2015**, *50*, 791–796. [CrossRef]
18. Kręcisz, M.; Rybka, J.D.; Strugała, A.J.; Skalski, B.; Figlerowicz, M.; Kozak, M.; Giersig, M. Interactions between magnetic nanoparticles and model lipid bilayers—Fourier transformed infrared spectroscopy (FTIR) studies of the molecular basis of nanotoxicity. *J. Appl. Phys.* **2016**, *120*, 124701. [CrossRef]
19. Haracz, S.; Hilgendorff, M.; Rybka, J.D.; Giersig, M. Effect of surfactant for magnetic properties of iron oxide nanoparticles. *Nucl. Instruments Methods Phys. Res. Sect. B Beam Interact. Mater. Atoms* **2015**, *364*, 120–126. [CrossRef]
20. Mahmoudi, M.; Sant, S.; Wang, B.; Laurent, S.; Sen, T. Superparamagnetic iron oxide nanoparticles (SPIONs): Development, surface modification and applications in chemotherapy. *Adv. Drug Deliv. Rev.* **2011**, *63*, 24–46. [CrossRef]
21. Neuberger, T.; Schöpf, B.; Hofmann, H.; Hofmann, M.; von Rechenberg, B. Superparamagnetic nanoparticles for biomedical applications: Possibilities and limitations of a new drug delivery system. *J. Magn. Magn. Mater.* **2005**, *293*, 483–496. [CrossRef]
22. Teja, A.S.; Koh, P.-Y. Synthesis, properties, and applications of magnetic iron oxide nanoparticles. *Prog. Cryst. Growth Charact. Mater.* **2009**, *55*, 22–45. [CrossRef]
23. Malyutin, A.G.; Easterday, R.; Lozovyy, Y.; Spilotros, A.; Cheng, H.; Sanchez-Felix, O.R.; Stein, B.D.; Morgan, D.G.; Svergun, D.I.; Dragnea, B.; et al. Viruslike nanoparticles with maghemite cores allow for enhanced mri contrast agents. *Chem. Mater.* **2015**, *27*, 327–335. [CrossRef]
24. Huang, X.; Bronstein, L.M.; Retrum, J.; Dufort, C.; Tsvetkova, I.; Aniagyei, S.; Stein, B.; Stucky, G.; McKenna, B.; Remmes, N.; et al. Self-assembled virus-like particles with magnetic cores. *Nano Lett.* **2007**, *7*, 2407–2416. [CrossRef] [PubMed]
25. Okuda, M.; Eloi, J.-C.; Jones, S.E.W.; Verwegen, M.; Cornelissen, J.J.L.M.; Schwarzacher, W. Pt, Co–Pt and Fe–Pt alloy nanoclusters encapsulated in virus capsids. *Nanotechnology* **2016**, *27*, 095605. [CrossRef]
26. Gubin, S.P.; Koksharov, Y.A.; Khomutov, G.B.; Yurkov, G.Y. Magnetic nanoparticles: preparation, structure and properties. *Russ. Chem. Rev.* **2005**, *74*, 489–520. [CrossRef]
27. Fatima, H.; Kim, K.S. Magnetic nanoparticles for bioseparation. *Korean J. Chem. Eng.* **2017**, *34*, 589–599. [CrossRef]
28. Shen, L.; Zhou, J.; Wang, Y.; Kang, N.; Ke, X.; Bi, S.; Ren, L. Efficient Encapsulation of Fe_3O_4 Nanoparticles into Genetically Engineered Hepatitis B Core Virus-Like Particles Through a Specific Interaction for Potential Bioapplications. *Small* **2015**, *11*, 1190–1196. [CrossRef]
29. Roose, K.; De Baets, S.; Schepens, B.; Saelens, X. Hepatitis B core-based virus-like particles to present heterologous epitopes. *Expert Rev. Vaccines* **2013**, *12*, 183–198. [CrossRef]
30. Belyi, V.A.; Muthukumar, M. Electrostatic origin of the genome packing in viruses. *Proc. Natl. Acad. Sci. USA* **2006**, *103*, 17174–17178. [CrossRef]

31. Mieloch, A.A.; Kręcisz, M.; Rybka, J.D.; Strugała, A.; Krupiński, M.; Urbanowicz, A.; Kozak, M.; Skalski, B.; Figlerowicz, M.; Giersig, M. The influence of ligand charge and length on the assembly of *Brome mosaic virus* derived virus-like particles with magnetic core. *AIP Adv.* **2018**, *8*, 035005. [CrossRef]
32. Giersig, M.; Hilgendorff, M. Magnetic nanoparticle superstructures. *Eur. J. Inorg. Chem.* **2005**, *2005*, 3571–3583. [CrossRef]
33. Peyret, H.; Lomonossoff, G.P. The pEAQ vector series: the easy and quick way to produce recombinant proteins in plants. *Plant Mol. Biol.* **2013**, *83*, 51–58. [CrossRef] [PubMed]
34. Pyrski, M.; Rugowska, A.; Wierzbiński, K.R.; Kasprzyk, A.; Bogusiewicz, M.; Bociąg, P.; Samardakiewicz, S.; Czyż, M.; Kurpisz, M.; Pniewski, T. HBcAg produced in transgenic tobacco triggers Th1 and Th2 response when intramuscularly delivered. *Vaccine* **2017**, *35*, 5714–5721. [CrossRef] [PubMed]
35. Hagan, M.F. A theory for viral capsid assembly around electrostatic cores. *J. Chem. Phys.* **2009**, *130*, 114902. [CrossRef] [PubMed]
36. Šiber, A.; Zandi, R.; Podgornik, R. Thermodynamics of nanospheres encapsulated in virus capsids. *Phys. Rev. E Stat. Nonlinear Soft Matter Phys.* **2010**, *81*, 051919. [CrossRef]
37. Wu, W.; Chen, Z.; Cheng, N.; Watts, N.R.; Stahl, S.J.; Farci, P.; Purcell, R.H.; Wingfield, P.T.; Steven, A.C. Specificity of an anti-capsid antibody associated with Hepatitis B Virus-related acute liver failure. *J. Struct. Biol.* **2013**, *181*, 53–60. [CrossRef]
38. Kent, S.P.; Ryan, K.H.; Siegel, A.L. Steric hindrance as a factor in the reaction of labeled antibody with cell surface antigenic determinants. *J. Histochem. Cytochem.* **1978**, *26*, 618–621. [CrossRef]
39. De Michele, C.; De Los Rios, P.; Foffi, G.; Piazza, F. Simulation and Theory of Antibody Binding to Crowded Antigen—Covered Surfaces. *PLoS Comput. Biol.* **2016**, *12*, e1004752. [CrossRef]
40. Hagan, M.F. Controlling viral capsid assembly with templating. *Phys. Rev. E Stat. Nonlinear Soft Matter Phys.* **2008**, *77*, 051904. [CrossRef]

© 2019 by the authors. Licensee MDPI, Basel, Switzerland. This article is an open access article distributed under the terms and conditions of the Creative Commons Attribution (CC BY) license (http://creativecommons.org/licenses/by/4.0/).

View publication stats

Journal of
Clinical Medicine

MDPI

Article

Osteoarthritis Severely Decreases the Elasticity and Hardness of Knee Joint Cartilage: A Nanoindentation Study

Adam Aron Mieloch [1,2,†], Magdalena Richter [1,†], Tomasz Trzeciak [3], Michael Giersig [1,4] and Jakub Dalibor Rybka [1,*]

1 Center for Advanced Technology, Adam Mickiewicz University in Poznan, Uniwersytetu Poznańskiego 10 Street, 61-614 Poznan, Poland; amieloch@amu.edu.pl (A.M.), magdalena.richter@amu.edu.pl (M.R.), giersig@amu.edu.pl (M.G.)
2 Faculty of Chemistry, Adam Mickiewicz University in Poznan, Uniwersytetu Poznańskiego 8 Street, 61-614 Poznan, Poland
3 Department of Orthopedics and Traumatology, Poznan University of Medical Sciences, 28 czerwca 1956r. Street No. 135/147, 61-545 Poznan, Poland; tomasz.trzeciak@ump.edu.pl
4 Department of Physics, Institute of Experimental Physics, Freie Universität, Arnimallee 14, 14195 Berlin, Germany; giersig@amu.edu.pl
* Correspondence: jrybka@amu.edu.pl; Tel.: +48-61-829-1875
† These authors contributed equally to this work.

Received: 16 September 2019; Accepted: 1 November 2019; Published: 3 November 2019

Abstract: The nanoindentation method was applied to determine the elastic modulus and hardness of knee articular cartilage. Cartilage samples from both high weight bearing (HWB) and low weight bearing (LWB) femoral condyles were collected from patients diagnosed with osteoarthritis (OA). The mean elastic modulus of HWB cartilage was 4.46 ± 4.44 MPa in comparison to that of the LWB region (9.81 ± 8.88 MPa, $p < 0.001$). Similarly, the hardness was significantly lower in HWB tissue (0.317 ± 0.397 MPa) than in LWB cartilage (0.455 ± 0.434 MPa, $p < 0.001$). When adjusted to patients' ages, the mean elastic modulus and hardness were both significantly lower in the age group over 70 years ($p < 0.001$). A statistically significant difference in mechanical parameters was also found in grade 3 and 4 OA. This study provides an insight into the nanomechanical properties of the knee articular cartilage and provides a starting point for personalized cartilage grafts that are compatible with the mechanical properties of the native tissue.

Keywords: articular cartilage; osteoarthritis; elastic modulus; mechanical properties; nanoindentation

1. Introduction

Articular cartilage (AC) is a highly specialized weight-bearing tissue that provides low friction during joint articulation. Due to its unique biomechanical functions, AC is mainly avascular, aneural, and alymphatic in structure and is capable of withstanding intensive cyclic loading and shear stress. The molecular composition of the AC perfectly reflects its physiological functions. It is composed of 70–80% water, 15% collagens (predominantly type II collagen), 9% aggrecan, and 3% chondrocytes. The cartilage matrix composition varies depending on the cartilage zone (i.e., tangential, transitional, radial, and calcified). Besides type II collagen, AC contains minute amounts of other types of collagen: III, VI, IX, XI, XII, and XIV [1]. Aggrecan is the main proteoglycan comprising two types of glycosaminoglycans (GAGs): chondroitin sulphate and keratin sulphate. GAGs are highly polyanionic and can bind up to 50 times their weight in water. This mechanism endows AC with its tensile strength, stiffness, and elasticity. The presence of structured collagen fibers and proteoglycans

reduces the friction of the articular surface and provides high resistance to mechanical stress, ensuring painless movement in the joints [2].

AC damage may occur either as a result of biological factors (e.g., imbalanced expression of cytokines) or mechanical factors [3]. Its avascular structure and low cellular content render AC incapable of efficient self-renewal [4,5]. Mechanical damage or progressing degradation results in numerous morphological, biochemical, and biophysical changes in cartilage structure [6]. Gradual deterioration is also a hallmark of osteoarthritis (OA) [7]. Cartilage erosion is thought to be caused by sustained imbalance between catabolic and anabolic processes. Increased activity of enzymes such as, e.g., matrix metalloproteinases (MMPs) contributes to extracellular matrix (ECM) breakdown. The erosion begins with the truncation of essential components such as collagens and aggrecans [8]. Due to proteoglycan loss, the most superficial cartilage zone (tangential) becomes fibrillated. The progression of matrix degradation results in increased water content and disruption of the collagen network, which, in turn, deteriorates the mechanical properties of the tissue and initiates the compensational synthesis of type II collagen [9]. Further alterations increase cartilage vulnerability to mechanical loads and lead to secondary changes such as subchondral bone sclerosis or osteophyte formation [10]. While the morphological and histological features of OA are well established, the underlying molecular mechanisms are still not completely understood. The mechanical characterization at the nano scale may provide important cues toward unraveling the molecular complexity of the disease.

Nanoindentation has been developed primarily for the nanomechanical characterization of non-biological surfaces. Paradoxically, limitations of this method stem from its high precision and accuracy. Pronounced heterogeneity of the biological surfaces' topography renders the utilization of this method quite challenging. Nonetheless, if applied properly, the method offers unmatched accuracy and provides a deep insight into the nanomechanical properties of a given tissue. Although other clinical indentation devices exist, they lack the sensitivity to expose local and distinct changes in the mechanical features of the AC [11].

A study by Stolz et al. inspired us to investigate the potential use of nanoindentation to reveal the discrete changes at the nanoscale occurring during the course of OA [12]. The majority of studies regarding the mechanical properties of AC have been based on intact (healthy) tissue [13–16]. Only a few experimental studies so far have characterized the properties of degenerated tissue [17–21]. Nia et al. investigated a murine femur cartilage elastic modulus and showed that aggrecan depletion led to a significant decrease in the elastic modulus from 2.0 MPa to around 0.4 MPa [17]. Furthermore, Doyran et al. observed, that in a murine post-traumatic model of OA, changes in cartilage mechanical properties markedly preceded the histological signs of the disease and were detectable at 1 week [22]. Interestingly, when the decrease in the elastic modulus was tested for the case of human osteoarthritic cartilage, it was not correlated with the disease progression [17]. Other studies indicated both an increase and decrease in cartilage elasticity during the course of OA [23,24]. It has been shown that the elastic modulus varies depending on the depth of the indent; therefore, each zone displays slightly different mechanical properties [16]. Similarly, different regions of the knee joint are exposed to different magnitudes of forces. Based on those differences, two types of regions could be distinguished—low weight bearing (LWB) and high weight bearing (HWB). Due to higher exposure to mechanical stress, the HWB region is more prone to the development of OA.

Regarding cartilage repair techniques, the difference between the mechanical properties of the LWB and HWB regions could eventually impact the outcome of AC repair. Differences in the mechanical characteristics between the tissue and a graft may impair its integration. Therefore, whether cell-loaded or cell-free, grafts and scaffolds should represent appropriate mechanical features to support the loading of the joint surfaces and thus easily integrate with the surrounding tissue.

Currently, there are no comprehensive studies on the mechanical properties of high weight bearing and low weight bearing articular cartilage at different stages of OA. This study describes the mechanical features of articular cartilage in terms of the hardness and elastic modulus. A novel

implementation of the nanoindentation technique provides an insight into the biomechanical properties of osteoarthritic cartilage.

2. Materials and Methods

2.1. Samples Collection

Samples of AC were harvested from 75 patients diagnosed with OA undergoing a total knee replacement procedure at the Department of Orthopedics and Traumatology, Poznan University of Medical Sciences. All subjects gave their informed consent for inclusion before they participated in the study. The study was conducted in accordance with the Declaration of Helsinki, and the protocol was approved by the Ethics Committee of Poznan University of Medical Sciences (permission No. 1016/16), and written consent from each patient was obtained.

The OA was diagnosed according to the American College of Rheumatology (ACR) criteria. The exclusion conditions included the presence of rheumatoid arthritis, osteotomy, and post-traumatic osteoarthritis. The radiological stage of the disease was evaluated according to the Kellgren–Lawrence (K-L) scale. The AC specimens were taken from both the medial and the lateral femoral condyle of each patient. Regarding the joint axial deformation (varus or valgus) and tissue morphology, samples were then marked as HWB or LWB (Figure 1).

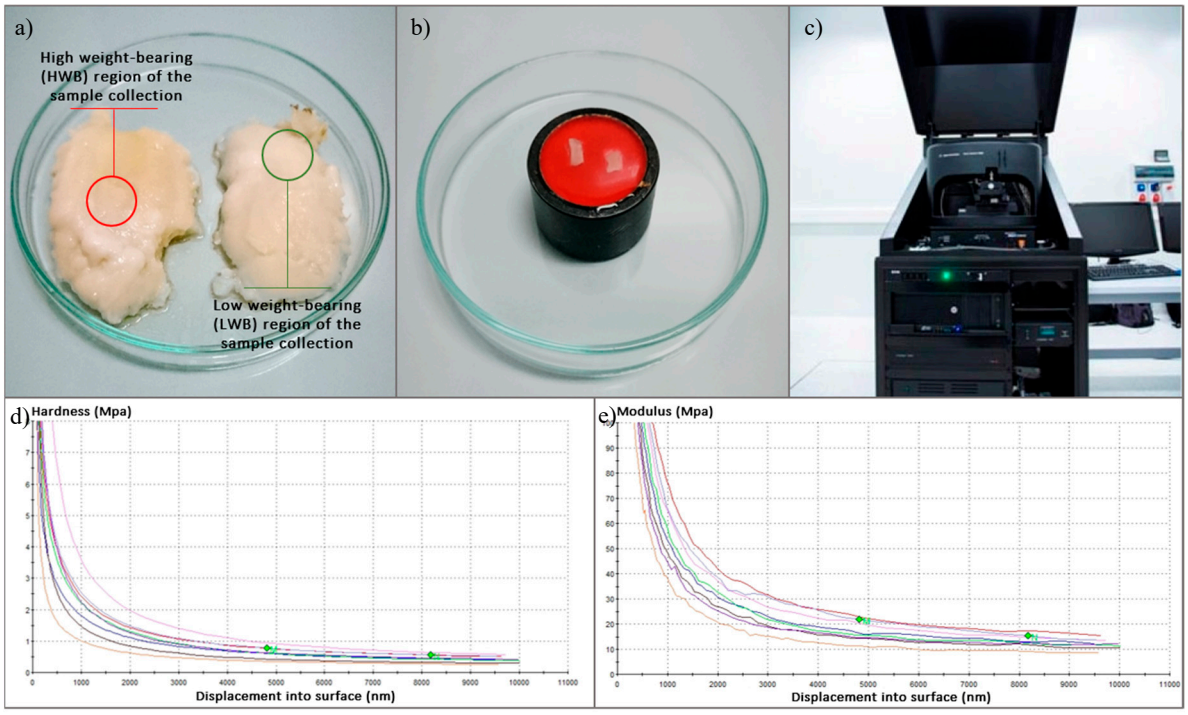

Figure 1. Graphical description of the experiment design: (**a**) indication of locations chosen for sample harvesting; (**b**) sample prepared for measurement; (**c**) nanoindenter used in the study; (**d**), (**e**) exemplary data obtained from the measurements.

2.2. Nanoindentation Measurements

The cartilage was cut with a surgical blade to obtain samples of at least 3.0 mm × 3.0 mm of flat surface. For the nanoindentation measurement, the AC samples were fixed in acrylic resin (Form Plast, Zhermapol®, Warsaw, Poland) to dedicated holders, with the superficial layer facing the indenter. After fixation, samples were rehydrated at RT with phosphate buffer saline (PBS) for 15 min. Before analysis, the excess PBS was poured onto the samples to prevent drying during measurement. The indentation tests were conducted on a nanoindenter Agilent G200 with a DCMII head (Agilent Technologies, Inc., Santa Clara, CA, USA) fitted with a Berkovich-type indenter tip (Figure 2). The area function was calculated according the formula

$$A(h_c) = m_0 + h_c^2 + m_1 + h_c + m_2 + h_c^{\left(\frac{1}{2}\right)} + \cdots + m_n + h_c^{\left(\frac{1}{2^{(n-1)}}\right)} \quad (1)$$

where the nominal value was m0 = 24.5.

The tip was calibrated before each sample measurement on quartz crystal (Young`s modulus E = 74 GPa). The measurements were performed in CSM mode (Continuous Stiffness Measurement). Indentations were performed at a depth of up to 10 μm with a strain rate of 1 [1/s] and a Poisson's ratio of 0.4. In order to calculate the Hardness and Elasticity modulus, determination of the elastic stiffness of the contact is required. Typically, it is derived from the slope of the load–displacement curve during the unload segment [25]. However, this calculation only gives the results for the maximum penetration depth. In our experimental setup, due to the continuous stiffness measurement technique (CSM), the measurement of the elastic stiffness of the contact (and thus the hardness and elasticity modulus) was obtained continuously during the loading. In CSM measurements, the additional harmonic force (with the amplitude in the range of nanometers) is added to the nominally increasing load. The displacement response of the indenter at this harmonic frequency can be analyzed in terms of the displacement amplitude, phase angle, and excitation amplitude. Solving the response equations (described elsewhere [26]) results in the determination of the elastic stiffness of the contact as a continuous function of the depth.

For each sample, 12 indents were performed in a 3 × 4 matrix with 200 μm x,y indent separation. The maximum depth of the indentation was 10.0 μm. The mean elastic modulus and hardness were obtained from the 5.0–8.0 μm indentation depth range. Exemplary raw data obtained from the measurements can be found in the Supplementary Material section (Figures S1–S6).

2.3. Histological Analysis

For histology, representative samples of the HWB articular cartilage of patients with K-L grades 2–4 were prepared for the experiments. Cartilage was harvested, fixed in 4% paraformaldehyde, decalcified in 12% EDTA, and embedded in parafin. Serial 5 μm thick sections were cut and stained with Safranin-O/Fast Green (Supplementary Material, Figure S7).

2.4. Statistical Analysis

Data were analyzed with Statistica version 13.1 (Tibco Software, Inc., Palo Alto, CA, USA). Descriptive statistics are reported as means, standard deviations (SD), medians, and minimum and maximum values. The Shapiro–Wilk test was used to assess the normality of distributions in the test score. If the data were normally distributed, parametric statistics were used for analyzing the data. The significance of the differences between the results of the tested and control sample was calculated using a paired t-test or non-parametric Wilcoxon signed-ranks test. The non-parametric Mann–Whitney test was conducted to compare the mean elastic modulus and hardness in patients divided by age and sex. The non-parametric Kruskal–Wallis test was used to analyze the differences between the mean elastic modulus and hardness in patients divided by BMI and Kellgren–Lawrence on more than two groups. The Dunn's post hoc test was used to show the difference between the tested groups. p-values of less than 0.05 were considered statistically significant.

3. Results

The anthropometric characteristics of the patients are summarized in Table 1. The evaluation of knee radiographs using the K-L grading system showed no patients graded 0, 16 patients graded 2, 39 patients graded 3, and 20 patients graded 4.

Table 1. Baseline demographics of the patients.

Variable	Mean ± SD	median	min–max
Age (years)	68.5 ± 7.5	69.0	52.0–82.0
Weight (kg)	84.0 ± 14.7	82.0	55.0–118.0
Height (cm)	163.8 ± 8.7	164.0	146.0–183.0
BMI (kg/m^2)	31.3 ± 5.0	31.0	22.0–46.1

BMI, body mass index; SD, standard deviation.

The mean elastic modulus and hardness of HWB cartilage (tested) were significantly lower, when compared to that of LWB (control) (Table 2). The relative frequency values of the mean elastic modulus and hardness obtained in both groups can be found in the Supplementary Materials section (Figure S8 and S9). The difference remained significant when estimated for males and females alone (Table 3). For tested samples, values were higher in females, while they were lower in the control tissue, when compared to males. However, when testing within the HWB and LWB groups of male and female samples, no significant differences were found (Supplementary Material, Table S1: Elastic modulus and hardness of HWB and LWB articular cartilage; adjusted to patients' sex tested within the groups).

Table 2. Elastic modulus and hardness of high weight bearing (HWB) and low weight bearing (LWB) articular cartilage.

	HWB cartilage			LWB cartilage			
Variable	**Mean ± SD**	**median**	**min–max**	**Mean ± SD**	**median**	**min-max**	***p*-value**
Elastic modulus (MPa)	4.46 ± 4.44	2.90	1.10–24.35	9.81 ± 8.88	7.40	1.10–51.00	<0.001*
Hardness (MPa)	0.317 ± 0.397	0.190	0.040–2.640	0.455 ± 0.434	0.320	0.060–2.200	<0.001*

*Wilcoxon signed-rank test.

Table 3. Elastic modulus and hardness of high weight bearing (HWB) and low weight bearing (LWB) articular cartilage adjusted to patients' sexes.

			HWB cartilage			LWB cartilage			
Variable	Sex	*n*	Mean ± SD	median	min–max	Mean ± SD	median	min–max	*p*-value
Elastic modulus (MPa)	Female	57	4.52 ± 4.17	2.94	1.10–19.70	9.54 ± 8.56	7.11	1.10–51.00	<0.001*
	Male	18	4.25 ± 5.34	2.60	1.30–24.35	10.66 ± 10.05	8.30	1.19–37.40	0.002*
Hardness (MPa)	Female	57	0.309 ± 0.318	0.200	0.040–1.570	0.442 ± 0.424	0.320	0.060–2.200	0.004*
	Male	18	0.343 ± 0.594	0.130	0.070–2.640	0.493 ± 0.478	0.330	0.060–2.000	0.022*

*Wilcoxon signed-rank test.

From the data shown in Table 4, it appears that there is a significant decline in the biomechanical properties of cartilage with increasing age. When adjusted to age, the mean elastic modulus and hardness of articular cartilage were significantly lower in the age group over 70 years (Table 4). These trends are shown in Figure 2; Figure 3, which present the combined sample mean and standard deviation plotted against the patients' ages.

Table 4. Elastic modulus and hardness of high weight bearing (HWB) and low weight bearing (LWB) articular cartilage adjusted to patients' ages.

			HWB cartilage			LWB cartilage			
Variable	Age	*n*	Mean ± SD	median	min–max	Mean ± SD	median	min–max	*p*-value
Elastic modulus (MPa)	<69	39	5.28 ± 5.50	2.94	1.22–24.35	8.24 ± 5.94	7.11	1.10–27.80	0,002*
	>70	36	3.56 ± 2.71	2.83	1.10–15.86	11.51 ± 11.07	8.18	2.13–51.00	<0.001*
Hardness (MPa)	<69	39	0,371 ± 0.480	0.210	0.070–2.640	0.389 ± 0.372	0.280	0.060–2.00	0.085*
	>70	36	0.259 ± 0.277	0.165	0.040–1.570	0.525 ± 0.489	0.390	0.100–2.100	<0.001*

*Wilcoxon signed-rank test

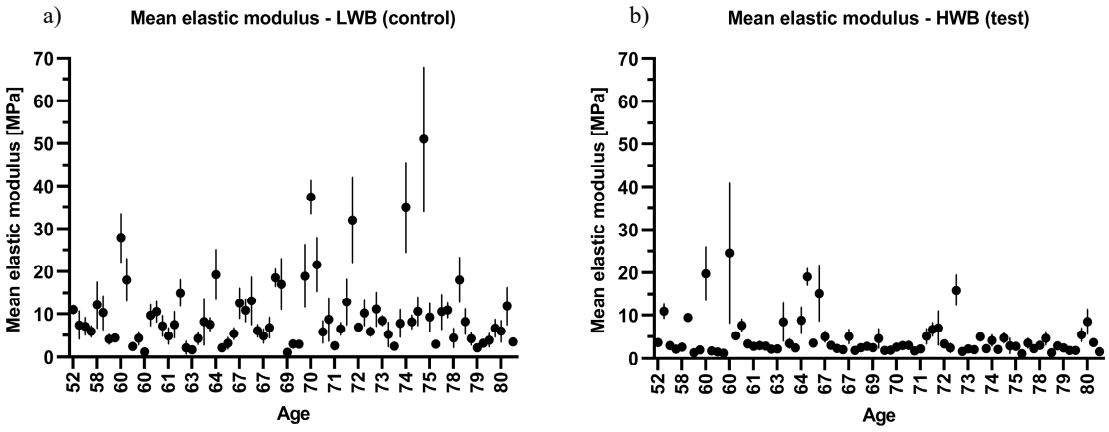

Figure 2. Scatter plot of the mean elastic modulus against age: (**a**) low weight bearing (LWB) sample and (**b**) high weight bearing (HWB) sample.

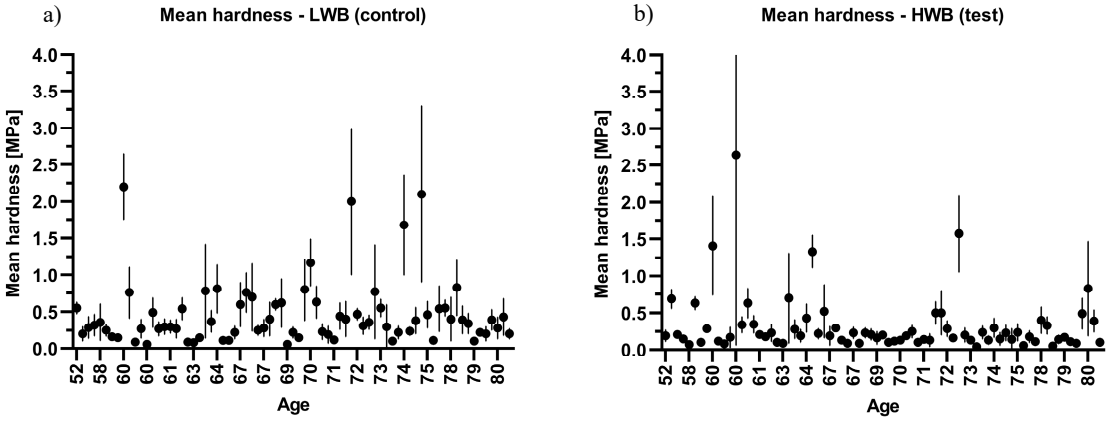

Figure 3. Scatter plot of hardness against age: (**a**) low weight bearing (LWB) sample and (**b**) high weight bearing (HWB) sample.

The evaluation of the biomechanical properties of articular cartilage in patients at different stages of OA revealed 2–3-fold lower values for grade 3 and 4 HWB sites in terms of the elastic modulus. For hardness, a statistically significant difference was found for grade 3 samples. No appreciable differences were found for grade 2 and 4 OA (Table 5).

Table 5. Elastic modulus and hardness of high weight bearing (HWB) and low weight bearing (LWB) articular cartilage adjusted to the Kellgren–Lawrence (K-L) osteoarthritis (OA) grading system.

			HWB cartilage			LWB cartilage			
Variable	K-L grade	*n*	Mean ± SD	median	min-max	Mean ± SD	median	min-max	*p*-value
Elastic modulus (MPa)	2	16	5.84 ± 5.04	3.76	1.70–18.99	11.32 ± 8.87	8.89	1.10–34.96	0.073
	3	39	3.78 ± 3.53	2.75	1.22–19.70	10.29 ± 9.90	8.13	1.67–51.00	<0.001*
	4	20	4.66 ± 5.42	2.59	1.10–24.35	7.66 ± 6.45	6.86	1.19–32.00	0.008*
Hardness (MPa)	2	16	0.416 ± 0.438	0.240	0.070–1.570	0.463 ± 0.391	0.370	0.060–1.680	0.772
	3	39	0.248 ± 0.230	0.190	0.050–1.410	0.481 ± 0.462	0.370	0.080–2.200	<0.001*
	4	20	0.375 ± 0.579	0.165	0.040–2.640	0.396 ± 0.426	0.285	0.060–2.000	0.179*

paired t-test, *Wilcoxon signed-rank test.

However, no statistically significant differences were found when the biomechanical parameters of the cartilage were grouped by patients' ages, sexes, BMI values, and OA grades and tested within the groups and between the groups (Table 6).

Table 6. Differences between the values of elastic modulus and hardness of high weight bearing (HWB) and low weight bearing (LWB) articular cartilage adjusted to age, sex, BMI, and the K-L OA grade tested within the groups and between the groups.

		HWB cartilage		LWB cartilage		HWB vs. LWB	
		Elastic modulus	Hardness	Elastic modulus	Hardness	Elastic modulus	Hardness
Age	<69 >70	0.311*	0.270*	0.270*	0.127*	0.124*	0.160*
Sex	f m	0.283*	0.208*	0.941*	0.936*	0.519*	0.355*
BMI	normal overweight obese	0.548**	0.406**	0.742**	0.738**	0.938**	0.991**
K-L grade	2 3 4	0.130**	0.365**	0.414**	0.482**	0.523**	0.688**

*Mann–Whitney U test, ** Kruskal–Wallis test.

Moreover, increasing age and OA grade were not correlated with the decrease of articular cartilage mechanical properties when analyzed within the HWB and LWB groups (Supplementary Material, Table S2: Correlations between high weight-bearing cartilage (HWB) and low weight-bearing cartilage (LWB) mechanical parameters and age or OA grade tested within the groups).

4. Discussion

Tissue engineering techniques permit an innovative approach to articular cartilage repair. However, information about the mechanical properties of human cartilage altered by joint degenerative disease is limited. AC is an inhomogeneous tissue, in which mechanical properties depend mostly on the ECM composition. Its biomechanical function is related to the water content and collagen, proteoglycans, and hyaluronate concentrations and to the interactions between these components. Consequently, alterations in the ECM components and disrupted tissue integrity, either by injury or disease, result in deterioration of the mechanical strength.

To our knowledge, this is one of the first studies of the nanomechanical properties of weight-bearing and non-weight-bearing articular cartilage at different stages of OA conducted at this scale. Researchers are consistent in the view that the elastic modulus of articular cartilage lies within the range of a few MPa [12,13,17,19,24]. The results of our work are commensurate with the previous studies, where the mechanical properties of articular cartilage were measured. Moshtagh et al. reported the average elastic modulus of the medial tibia plateau cartilage as being 2.6 ± 1.4 MPa, while that of the lateral tibia was reported as being 4.2 ± 2.6 MPa [27]. Antons et al. observed values

ranging from 0.020 ± 0.003 MPa in the superficial zone to 6.44 ± 1.02 MPa in the calcified zone of human femoral condyle cartilage [16]. Other researchers have presented contradictory results. Sergerie et al. showed that ECM stiffness decreases along the cartilage zones of the porcine cartilage growth plate, while Park et al. showed that rabbit growth plate stiffness increases across the same region [28,29]. Therefore, site-specific properties, local variation, and cartilage sample thickness should not be neglected [30–32]. Observed discrepancies in the values of hardness and elastic modulus could stem from measuring different cartilage zones, which was unavoidable due to inhomogeneous structure of the osteoarthritic cartilage. Moreover, it seems that nanoscale indentation with sharp probes picks up the mechanics of individual macromolecules and is reflected the elasticity of collagen or aggrecan macromolecules [11,33,34]. Chandran et al. stated that an indentation depth of at least 0.6 μm is required to obtain values of matrix elasticity, instead of a rough superficial layer [14]. In the study by Antons et al., the thickness of the samples ranged from 1484 ± 75.23 μm to 3624.4 ± 164.11 μm [16]. In a study by Moshtagh et al., it was observed that each 60 μm change in indenter location could result in a 20-fold variation in the measurement [27].

Values reported by others, suggest, that our measurements were taken in the deep layers of cartilage, rather than in the superficial zone. Additionally, measuring the superficial layer would be very challenging, since the samples were harvested from donors diagnosed with OA. In general, special care was taken to harvest the samples from precisely the same area of the femoral condyle. Nevertheless, the disease stage could influence the accessibility of the tissue, especially from the HWB region of the cartilage. Despite some technical difficulties, our study revealed a significant decrease in the biomechanical properties of the articular cartilage associated with age and disease progression. We observed a 2–3-fold decrease in the elastic modulus and the hardness of cartilage in patients over 70 years of age. Similarly, a significant deterioration of the parameters was observed in stages 2 to 4 of OA. Peters et al. also found that increasing age and OA grade were strongly correlated with a decrease in cartilage shear modulus ($p = 0.003$ and $p = 0.007$, respectively) [20]. Cao et al. noticed that the decreased stiffness of the OA cartilage may be caused by increased water content and elevated permeability as well as to a decreased proteoglycans content [13]. Nia et al. found that aggrecan depletion from a mouse femur led to a significant decrease in the elastic modulus (from approx. 2.0 to 0.4 MPa). However, the aggrecan depletion was not observed for human cartilage in correlation to the progression of OA [17].

In spite of the intriguing results, there were several limitations in our study. First of all, a biochemical analysis was not performed to elucidate the cartilage composition and its correlation with the mechanical properties of the tissue. Another limitation is the lack of an appropriate reference material, such as a cartilage sample from a healthy donor, which may have provided comparative values of measured parameters and the extent of the impact of OA on the articular cartilage biomechanics. This, however, could be done in the future using cadaver cartilage taken from young subjects. Moreover, the indenter tip used in this study (Berkovich type) could influence the materials' behavior under indentation. This is related to the size of the indentation region, which is different in cases of Berkovich and conical tips [35]. However, for biological samples, a spherical indentation tip is more commonly used, due to its more favorable geometry, providing a good alignment between the indenter and the material surface [36,37].

5. Conclusions

This study demonstrates the regional mechanical properties of the articular cartilage of the knee joint taken from a representative number of OA patients. The results provide insight into the mechanical behavior of the cartilage at different stages of OA in correlation to the patients' ages, which is essential from the clinical perspective. Matching the mechanical characteristics of the tissue and graft is crucially important for proper integration with the surrounding tissue [38–41]. Currently, there are no methods to select an ideal biomaterial-based graft for repairing cartilage lesions. Moreover, the repair procedures are mostly performed on the high weight-bearing surface of the femoral condyle, thus indicating the importance of assessing the biomechanical properties of

surrounding tissue prior to graft implantation. This would significantly raise the chances for successful and long-term clinical improvement of the operated patients.

Supplementary Materials: The following are available online at www.mdpi.com/xxx/s1, Figure S1: Exemplary raw data obtained from the measurements; Figure S2: Exemplary raw data obtained from the measurements; Figure S3: Exemplary raw data obtained from the measurements; Figure S4: Exemplary raw data obtained from the measurements; Figure S5: Exemplary raw data obtained from the measurements; Figure S6: Exemplary raw data obtained from the measurements; Figure S7: Representative histology sections of HWB cartilage (Safranin-O/Fast Green staining); Figure S8: Relative frequency of mean elastic modulus of: (a) low weight bearing (LWB) sample and (b) high weight bearing (HWB) sample; Figure S9: Relative frequency of mean hardness of: (a) low weight bearing (LWB) sample and (b) high weight bearing (HWB) sample. Table S1: Elastic modulus and hardness of high weight bearing (HWB) and low weight bearing (LWB) articular cartilage; adjusted to patients' sex tested within the groups, Table S2: Correlations between high weight bearing cartilage (HWB) and low weight bearing cartilage (LWB) mechanical parameters and age or OA grade tested within the groups.

Author Contributions: Conceptualization, A.M., M.R. and J.D.R.; Data curation, A.M.; Formal analysis, M.R.; Funding acquisition, J.D.R.; Investigation, A.M.; Methodology, A.M., M.R. and J.D.R.; Project administration, J.D.R.; Supervision, M.G. and J.D.R.; Validation, M.R. and J.D.R.; Writing—original draft, A.M. and M.R.; Writing—review & editing, T.T. and J.D.R.

Acknowledgements: We would like to thank Łukasz Majchrzycki for his valuable insights and contribution to nanoindentation analysis.

Funding: This work was supported by the National Centre for Research and Development LIDER/34/0122/L-9/17/NCBR/2018 and the National Science Centre UMO-2016/23/B/NZ7/01288 grants. The work was supported by grant no. POWR.03.02.00-00-I026/16 co-financed by the European Union through the European Social Fund under the Operational Program Knowledge Education Development

Conflicts of Interest: The authors declare no conflict of interest.

References

1. Aigner, T.; Stöve, J. Collagens—Major component of the physiological cartilage matrix, major target of cartilage degeneration, major tool in cartilage repair. *Adv. Drug Deliv. Rev.* **2003**, *55*, 1569–1593.
2. Sophia Fox, A.J.; Bedi, A.; Rodeo, S.A. The basic science of articular cartilage: Structure, composition, and function. *Sports Health* **2009**, *1*, 461–468.
3. Richter, M.; Trzeciak, T.; Rybka, J.D.; Suchorska, W.; Augustyniak, E.; Lach, M.; Kaczmarek, M.; Kaczmarczyk, J. Correlations between serum adipocytokine concentrations, disease stage, radiologic status and total body fat content in the patients with primary knee osteoarthritis. *Int. Orthop.* **2017**, *41*, 983–989. doi:10.1007/s00264-016-3370-5.
4. Buckwalter, J.A.; Mow, V.C.; Ratcliffe, A. Restoration of Injured or Degenerated Articular Cartilage. *J. Am. Acad. Orthop. Surg.* **1994**, *2*, 192–201.
5. Buckwalter, J.A. Articular Cartilage: Injuries and Potential for Healing. *J. Orthop. Sport Phys. Ther.* **1998**, *28*, 192–202.
6. Buckwalter, J.A.; Saltzman, C.; Brown, T. The impact of osteoarthritis: Implications for research. *Clin. Orthop. Relat. Res.* **2004**, *427*, S6– S15.
7. Kean, W.F.; Kean, R.; Buchanan, W.W. Osteoarthritis: Symptoms, signs and source of pain. *Inflammopharmacology* **2004**, *12*, 3–31.
8. Goldring, M.B.; Marcu, K.B. Cartilage homeostasis in health and rheumatic diseases. *Arthritis Res. Ther.* **2009**, *11*, 224. doi:10.1186/ar2592.
9. Grimmer, C.; Balbus, N.; Lang, U.; Aigner, T.; Cramer, T.; Müller, L.; Swoboda, B.; Pfander, D. Regulation of type II collagen synthesis during osteoarthritis by prolyl-4-hydroxylases: Possible influence of low oxygen levels. *Am. J. Pathol.* **2006**, *169*, 491–502.
10. Buckwalter, J.A.; Mankin, H.J. Articular cartilage: Tissue design and chondrocyte-matrix interactions. *Instr. Course Lect.* **1998**, *47*, 477–486.
11. Stolz, M.; Raiteri, R.; Daniels, A.U.; VanLandingham, M.R.; Baschong, W.; Aebi, U. Dynamic elastic modulus of porcine articular cartilage determined at two different levels of tissue organization by indentation-type atomic force microscopy. *Biophys. J.* **2004**, *86*, 3269–3283.

12. Stolz, M.; Gottardi, R.; Raiteri, R.; Miot, S.; Martin, I.; Imer, R.; Staufer, U.; Raducanu, A.; Düggelin, M.; Baschong, W.; et al. Early detection of aging cartilage and osteoarthritis in mice and patient samples using atomic force microscopy. *Nat. Nanotechnol.* **2009**, *4*, 186–192. doi:10.1038/nnano.2008.410.
13. Cao, L.; Youn, I.; Guilak, F.; Setton, L.A. Compressive properties of mouse articular cartilage determined in a novel micro-indentation test method and biphasic finite element model. *J. Biomech. Eng.* **2006**, *128*, 766–771.
14. Chandran, P.L.; Dimitriadis, E.K.; Mertz, E.L.; Horkay, F. Microscale mapping of extracellular matrix elasticity of mouse joint cartilage: An approach to extracting bulk elasticity of soft matter with surface roughness. *Soft Matter* **2018**, *14*, 2879–2892. doi:10.1039/c7sm02045g.
15. Wahlquist, J.A.; DelRio, F.W.; Randolph, M.A.; Aziz, AH.; Heveran, C.M.; Bryant, S.J.; Neu, C.P.; Ferguson, V.L. Indentation mapping revealed poroelastic, but not viscoelastic, properties spanning native zonal articular cartilage. *Acta Biomater.* **2017**, *64*, 41–49. doi:10.1016/j.actbio.2017.10.003.
16. Antons, J.; Marascio, M.G.M.; Nohava, J.; Martin, R.; Applegate, L.A.; Bourban, P.E.; Pioletti, D.P. Zone-dependent mechanical properties of human articular cartilage obtained by indentation measurements. *J. Mater. Sci. Mater. Med.* **2018**, *29*, 57. doi:10.1007/s10856-018-6066-0.
17. Nia, H.T.; Gauci, S.J.; Azadi, M.; Hung, H.H.; Frank, E.; Fosang, A.J.; Ortiz, C.; Grodzinsky, A.J. High-bandwidth AFM-based rheology is a sensitive indicator of early cartilage aggrecan degradation relevant to mouse models of osteoarthritis. *J. Biomech.* **2015**, *48*, 162–165. doi:10.1016/j.jbiomech.2014.11.012.
18. Robinson, D.L.; Kersh, M.E.; Walsh, N.C.; Ackland, D.C.; de Steiger, R.N.; Pandy, M.G. Mechanical properties of normal and osteoarthritic human articular cartilage. *J. Mech. Behav. Biomed. Mater.* **2016**, *61*, 96–109. doi:10.1016/j.jmbbm.2016.01.015.
19. Arabshahi, Z.; Afara, I.O.; Moody, H.R.; Schrobback, K.; Kashani, J.; Fischer, N.; Oloyede, A.; Klein, T.J. A new mechanical indentation framework for functional assessment of articular cartilage. *J. Mech. Behav. Biomed. Mater.* **2018**, *81*, 83–94. doi:10.1016/j.jmbbm.2018.02.028.
20. Peters, A.E.; Akhtar, R.; Comerford, E.J.; Bates, K.T. The effect of ageing and osteoarthritis on the mechanical properties of cartilage and bone in the human knee joint. *Sci. Rep.* **2018**, *8*, 5931. doi:10.1038/s41598-018-24258-6.
21. Marchi, G.; Foehr, P.; Consalvo, S.; Javadzadeh-Kalarhodi, A.; Lang, J.; Hartmann, B.; Alberton, P.; Aszodi, A.; Burgkart, R.; Roths, J. Fiberoptic microindentation technique for early osteoarthritis diagnosis: An in vitro study on human cartilage. *Biomed. Microdevices* **2019**, *21*, 11. doi:10.1007/s10544-019-0359-z.
22. Doyran, B.; Tong, W.; Li, Q.; Jia, H.; Zhang, X.; Chen, C.; Enomoto-Iwamoto, M.; Lu, X.L.; Qin, L.; Han, L. Nanoindentation modulus of murine cartilage: A sensitive indicator of the initiation and progression of post-traumatic osteoarthritis. *Osteoarthr. Cartil.* **2017**, *25*, 108–117. doi:10.1016/j.joca.2016.08.008.
23. Coles, J.M.; Zhang, L.; Blum, J.J.; Warman, M.L.; Jay, G.D.; Guilak, F.; Zauscher, S. Loss of cartilage structure, stiffness, and frictional properties in mice lacking PRG4. *Arthritis Rheum.* **2010**, *62*, 1666–1674. doi:10.1002/art.27436.
24. Candela, M.E.; Wang, C.; Gunawardena, A.T.; Zhang, K.; Cantley, L.; Yasuhara, R.; Usami, Y.; Francois, N.; Iwamoto, M.; van der Flier, A.; et al. Alpha 5 integrin mediates osteoarthritic changes in mouse knee joints. *PLoS ONE* **2016**, *11*, e0156783. doi:10.1371/journal.pone.0156783.
25. Fischer-Cripps, A.C. Critical review of analysis and interpretation of nanoindentation test data. *Surf. Coat. Technol.* **2006**, *200*, 4153–4165. doi:10.1016/j.surfcoat.2005.03.018.
26. Li, X.; Bhushan, B. A review of nanoindentation continuous stiffness measurement technique and its applications. *Mater. Charact.* **2002**, *48*, 11–36. doi:10.1016/S1044-5803(02)00192-4.
27. Moshtagh, P.R.; Pouran, B.; Korthagen, N.M.; Zadpoor, A.A.; Weinans, H. Guidelines for an optimized indentation protocol for measurement of cartilage stiffness: The effects of spatial variation and indentation parameters. *J. Biomech.* **2016**, *49*, 3602–3607. doi:10.1016/j.jbiomech.2016.09.020.
28. Sergerie, K.; Lacoursière, M.O.; Lévesque, M.; Villemure, I. Mechanical properties of the porcine growth plate and its three zones from unconfined compression tests. *J. Biomech.* **2009**, *42*, 510–516. doi:10.1016/j.jbiomech.2008.11.026.
29. Park, S.; Hung, C.T.; Ateshian, G.A. Mechanical response of bovine articular cartilage under dynamic unconfined compression loading at physiological stress levels. *Osteoarthr. Cartil.* **2004**, *12*, 65–73.
30. Jurvelin, J.S.; Arokoski, J.P.A.; Hunziker, E.B.; Helminen, H.J. Topographical variation of the elastic properties of articular cartilage in the canine knee. *J. Biomech.* **2000**, *33*, 669–675.

31. Hamann, N.; Brüggemann, G.P.; Niehoff, A. Topographical variations in articular cartilage and subchondral bone of the normal rat knee are age-related. *Ann. Anat.* **2014**, *196*, 278–285. doi:10.1016/j.aanat.2014.04.006.
32. Shekhawat, V.K.; Laurent, M.P.; Muehleman, C.; Wimmer, M.A. Surface topography of viable articular cartilage measured with scanning white light interferometry. *Osteoarthr. Cartil.* **2009**, *17*, 1197–1203. doi:10.1016/j.joca.2009.03.013.
33. Loparic, M.; Wirz, D.; Daniels, A.U.; Raiteri, R.; Vanlandingham, M.R.; Guex, G.; Martin, I.; Aebi, U.; Stolz, M. Micro- and nanomechanical analysis of articular cartilage by indentation-type atomic force microscopy: Validation with a gel-microfiber composite. *Biophys. J.* **2010**, *98*, 2731–2740. doi:10.1016/j.bpj.2010.02.013.
34. Prein, C.; Warmbold, N.; Farkas, Z.; Schieker, M.; Aszodi, A.; Clausen-Schaumann, H. Structural and mechanical properties of the proliferative zone of the developing murine growth plate cartilage assessed by atomic force microscopy. *Matrix Biol.* **2016**, *50*, 1–15. doi:10.1016/j.matbio.2015.10.001.
35. Sakharova, N.A.; Fernandes, J.M.; Antunes, J.M.; Oliveira, M.C. Comparison between Berkovich, Vickers and conical indentation tests: A three-dimensional numerical simulation study. *Int. J. Solids Struct.* **2009**, *46*, 1095–1104. doi:10.1016/j.ijsolstr.2008.10.032.
36. Cheng, L.; Xia, X.; Scriven, L.E.; Gerberich, W.W. Spherical-tip indentation of viscoelastic material. *Mech. Mater.* **2005**, *37*, 213–226.
37. Qian, L.; Zhao, H. Nanoindentation of Soft Biological Materials. *Micromachines (Basel)* **2018**, *9*, 654. doi:10.3390/mi9120654.
38. Trzeciak, T.; Rybka, J.D.; Akinoglu, E.; Richter, M.; Kaczmarczyk, J.; Giersig, M. In vitro evaluation of carbon nanotube-based scaffolds for cartilage tissue engineering. *J. Nanosci. Nanotechnol.* **2016**, *16*, 9022–9025. doi:10.1166/jnn.2016.12733.
39. Trzeciak, T.; Rybka, J.D.; Richter, M.; Kaczmarczyk, J.; Ramalingam, M.; Giersig. M. Cells and nanomaterial-based tissue engineering techniques in the treatment of bone and cartilage injuries. *J. Nanosci. Nanotechnol*. **2016**, *16*, 8948–8952.
40. Hassan, C.R.; Qin, Y.X.; Komatsu, D.E.; Uddin, S.M.Z. Utilization of Finite Element Analysis for Articular Cartilage Tissue Engineering. *Materials* **2019**, *12*, 3331. doi:10.3390/ma12203331.
41. Oliveira, A.S.; Seidi, O.; Ribeiro, N.; Colaço, R.; Serro, A.P. Tribomechanical Comparison between PVA Hydrogels Obtained Using Different Processing Conditions and Human Cartilage. *Materials* **2019**, *12*, 3413. doi:10.3390/ma12203413.

© 2019 by the authors. Licensee MDPI, Basel, Switzerland. This article is an open access article distributed under the terms and conditions of the Creative Commons Attribution (CC BY) license (http://creativecommons.org/licenses/by/4.0/).

View publication stats